



**NAVAL
POSTGRADUATE
SCHOOL**

MONTEREY, CALIFORNIA

THESIS

**TRANSPORT IMAGING FOR THE STUDY OF
QUANTUM SCATTERING PHENOMENA IN NEXT
GENERATION SEMICONDUCTOR DEVICES**

by

Frank Mitchell Bradley

December 2005

Thesis Advisor:
Second Reader:

Nancy M. Haegel
James Luscombe

Approved for public release; distribution is unlimited

THIS PAGE INTENTIONALLY LEFT BLANK

REPORT DOCUMENTATION PAGE

Form Approved OMB No. 0704-0188

Public reporting burden for this collection of information is estimated to average 1 hour per response, including the time for reviewing instruction, searching existing data sources, gathering and maintaining the data needed, and completing and reviewing the collection of information. Send comments regarding this burden estimate or any other aspect of this collection of information, including suggestions for reducing this burden, to Washington headquarters Services, Directorate for Information Operations and Reports, 1215 Jefferson Davis Highway, Suite 1204, Arlington, VA 22202-4302, and to the Office of Management and Budget, Paperwork Reduction Project (0704-0188) Washington DC 20503.

1. AGENCY USE ONLY (Leave blank)	2. REPORT DATE	3. REPORT TYPE AND DATES COVERED Master's Thesis	
4. TITLE AND SUBTITLE: Transport Imaging for the Study of Quantum Scattering Phenomena in Next Generation Semiconductor Devices		5. FUNDING NUMBERS	
6. AUTHOR(S) Frank Mitchell Bradley			
7. PERFORMING ORGANIZATION NAME(S) AND ADDRESS(ES) Naval Postgraduate School Monterey, CA 93943-5000		8. PERFORMING ORGANIZATION REPORT NUMBER	
9. SPONSORING /MONITORING AGENCY NAME(S) AND ADDRESS(ES) National Science Foundation Research Corporation CC4411		10. SPONSORING/MONITORING AGENCY REPORT NUMBER DMR 20033397	
11. SUPPLEMENTARY NOTES The views expressed in this thesis are those of the author and do not reflect the official policy or position of the Department of Defense or the U.S. Government.			
12a. DISTRIBUTION / AVAILABILITY STATEMENT Approved for public release; distribution is unlimited		12b. DISTRIBUTION CODE	
13. ABSTRACT (maximum 200 words) The minority carrier diffusion length is a critical parameter in the development of next generation Heterostructure Bipolar Transistors (HBT) and highly efficient solar cells. A novel technique has been developed utilizing direct imaging of electron/hole recombination via an optical microscope and a high sensitivity charge coupled device coupled to a scanning electron microscope to capture spatial information about the transport behavior (diffusion lengths/drift lengths) in luminescent solid state materials. In this work, a numerical model was developed to do a multi-parameter least squares analysis of transport images. Results were applied to the study of transport in materials at the forefront of device technology that are affected by quantum scattering effects, where few reliable experimental measurements exist. The technique allows for easy localization of the measurement site, broad application to a range of materials and potential industrial automation to aid the development of high speed electronics for terahertz devices.			
14. SUBJECT TERMS Minority carrier diffusion length, heterostructure bipolar transistors, transport imaging, heavily doped GaAs transport properties		15. NUMBER OF PAGES 113	
16. PRICE CODE			
17. SECURITY CLASSIFICATION OF REPORT Unclassified	18. SECURITY CLASSIFICATION OF THIS PAGE Unclassified	19. SECURITY CLASSIFICATION OF ABSTRACT Unclassified	20. LIMITATION OF ABSTRACT UL

NSN 7540-01-280-5500

Standard Form 298 (Rev. 2-89)
Prescribed by ANSI Std. Z39-18

THIS PAGE INTENTIONALLY LEFT BLANK

Approved for public release; distribution is unlimited

**TRANSPORT IMAGING FOR THE STUDY OF QUANTUM SCATTERING
PHENOMENA IN NEXT GENERATION SEMICONDUCTOR DEVICES**

Frank M. Bradley
Lieutenant Commander, United States Navy
B.S., United States Naval Academy, 1991

Submitted in partial fulfillment of the
requirements for the degree of

MASTER OF SCIENCE IN PHYSICS

from the

NAVAL POSTGRADUATE SCHOOL
December 2005

Author: Frank Mitchell Bradley

Approved by: Nancy M. Haegel
Thesis Advisor

James Luscombe
Second Reader

James Luscombe
Chairman, Department of Physics

THIS PAGE INTENTIONALLY LEFT BLANK

ABSTRACT

The minority carrier diffusion length is a critical parameter in the development of next generation Heterostructure Bipolar Transistors (HBT) and highly efficient solar cells. A novel technique has been developed utilizing direct imaging of electron/hole recombination via an optical microscope and a high sensitivity charge coupled device coupled to a scanning electron microscope to capture spatial information about the transport behavior (diffusion lengths/drift lengths) in luminescent solid state materials. In this work, a numerical model was developed to do a multi-parameter least squares analysis of transport images. Results were applied to the study of transport in materials at the forefront of device technology that are affected by quantum scattering effects, where few reliable experimental measurements exist. The technique allows for easy localization of the measurement site, broad application to a range of materials and potential industrial automation to aid the development of high speed electronics for terahertz devices.

THIS PAGE INTENTIONALLY LEFT BLANK

TABLE OF CONTENTS

I.	INTRODUCTION	1
A.	HISTORY	1
B.	MILITARY RELEVANCE	4
C.	THESIS OVERVIEW	5
II.	TRANSPORT IMAGING IN THE TWO DIMENSIONAL LIMIT	7
A.	OVERVIEW	7
B.	MODELING LIMITATIONS AND ASSUMPTIONS	7
C.	MATHEMATICAL MODEL DEVELOPMENT	8
1.	Generation Region	11
2.	Green's Function Solution	13
III.	EXPERIMENTAL APPARATUS	17
A.	INTRODUCTION	17
B.	APPARATUS DESCRIPTION	17
C.	DATA EXTRACTION	21
1.	Slope Analysis Estimation	22
2.	Least Squares 2-Parameter Fit Analysis	26
IV.	TRANSPORT IMAGING PREDICTIONS AND LIMITATIONS	29
A.	ERROR ESTIMATION FOR CURVE FITTING ALGORITHM	29
B.	LIMITS OF MODEL ASSUMPTIONS	35
1.	Low Injection Assumption	35
2.	Slope Analysis Limitations and the Low Injection Limit	37
3.	Small Diffusion Length Limitations and the Role of the Generation Distribution	41
V.	STUDY OF HEAVILY DOPED HETEROSTRUCTURES	45
A.	MOTIVATION	45
B.	QUANTUM MECHANICAL PREDICTIONS	46
C.	EXPERIMENTAL RESULTS	47
1.	Initial Observations	49
2.	Generation Region Discrepancies	50
C.	CORRECTIONS FOR OPERATIVE EFFECTS AND DISCUSSED LIMITATIONS	55
D.	CONCLUSIONS	56
APPENDIX A.	TRANSPORT IMAGING GRAPHIC USER INTERFACE CODE ..	59
APPENDIX B.	IMAGE DATA EXTRACTION ROUTINE (IMAGE DATAMANIPULATOR.M)	67
APPENDIX C.	LEAST SQUARES FIT ALGORITHM (FBSLD.M)	75

APPENDIX D. VECTOR DATA EXTRACTION ROUTINE "VDATAMANIPULATOR.M"	81
APPENDIX E. SLOPE ANALYSIS ALGORITHM (SLOPEL2.M)	85
APPENDIX F. NUMERICAL INTEGRATION SOLUTION FOR MINORITY CARRIER DISTRIBUTION (INTEGRAND.M)	89
APPENDIX G. PHOTON RECYCLING PERTURBATION	91
LIST OF REFERENCES	93
INITIAL DISTRIBUTION LIST	97

LIST OF FIGURES

Figure 1. (a) Schematic cross section of an HBT structure.	
(b) Energy band diagram of a HBT operated under active mode. (From Ref.[1])	2
Figure 2. Trend of best achieved F_t for various transistors. (From Ref[4])	3
Figure 3. E-Beam/Sample interaction schematic	9
Figure 4. Transport Imaging System Schematic	18
Figure 5. CCD image of Experimental Sample	21
Figure 7. Slope Analysis for Experimental Sample	23
Figure 8. Slope Analysis resolution	24
Figure 9. Slope Method Assumption Dependence on large Bessel Function argument	25
Figure 10. Least Squares Model Fit of Experimental Data	27
Figure 11. Baseline calculation error in Model Fit algorithm (no variation of integration step size) ..	31
Figure 12. Baseline calculation error in Model Fit algorithm (variation of integration step)	32
Figure 13. Error estimation for $0.1\mu m$ variation in Diffusion Length RMSE= 6.2×10^{-3}	33
Figure 15. Error estimation for $0.01\mu m$ variation in Generation Region radius RMSE= 2.5×10^{-3}	34
Figure 16. Error estimation for $0.2\mu m$ variation in Generation Region radius RMSE= 10.5×10^{-3}	34
Figure 17. AlGaAs/GaAs Heterostructure design from Tom Boone Doctoral Dissertation [22]	36
Figure 18. Slope and Model fit analysis plots for $6 \times 10^{-12} A$ probe current (pertinent data tabulated in Table 3)	39
Figure 19. Slope and Model fit analysis plots for $6 \times 10^{-11} A$ probe current (pertinent data tabulated in Table 3)	39
Figure 20. Slope and Model fit analysis plots for $6 \times 10^{-10} A$ probe current (pertinent data tabulated in Table 3)	40
Figure 21. Slope and Model fit analysis plots for $6 \times 10^{-9} A$ probe current (pertinent data tabulated in Table 3)	40
Figure 22. Slope and Model fit analysis plots for $6 \times 10^{-8} A$ probe current (pertinent data tabulated in Table	

3)	41
Figure 23. Pure Gaussian Distribution Model Fit	43
Figure 24. Heterostructure design as grown by Tom Boone, (From Ref. [22])	48
Figure 25. Samples A2 and B7 best fit 2-parameter fit extractions	50
Figure 26. Samples D6 and E3 best fit 2-parameter fit extractions	51
Figure 27. Sample F4 best fit 2-parameter fit extraction	51
Figure 28. Sample G8 best fit (a) algorithm run, (b) Assumed reasonable generation region with algorithm fitted diffusion length	51
Figure 29. Final corrected Transport Imaging mobility values reported (After Bennett [9])	57

LIST OF TABLES

Table 1.	Table 1. JEOL 840A Specifications (From [11])	19
Table 2.	Tabulated Error Estimates for Curve Fits	35
Table 3.	Measurement Results for $0.1\mu m$ active layer, Boone Heterostructure #9	37
Table 4.	Initial results of AlGaAs/GaAs heterostructure study	49
Table 5.	HS data table with absorption length comparison ..	54
Table 6.	Tabulated Parameters corrected for Generation Region error(**) and Photon Recycling overestimation	56

THIS PAGE INTENTIONALLY LEFT BLANK

ACKNOWLEDGMENTS

Though times are good or be they unknowable
The names to be trusted are always the same.
A family as steady as the Redwoods of ages.
A God more present than the mind can conceive.
Friends and mentors in a variety of manners,
Have touched me in ways too deep to perceive.

A word to all who read this in wonder,
"Why would a man care so for science?"

For I have seen good and bad in abundance.
The good, more often, was forgotten by most,
But the evil withstands and calls us each one.
It either is answered or followed asunder.
And ignorance is surely the path of the latter.

I acknowledge those who will not stand idle.
I acknowledge those who are pressed to act.
I acknowledge those who in their dying,
Have given me life of spirit and mind.
I acknowledge those who have gone before me
Great warriors, scholars, kith and kin.

THIS PAGE INTENTIONALLY LEFT BLANK

I. INTRODUCTION

A. HISTORY

With the emergence of the transistor in 1947 came a revolution in military affairs (RMA) that has been evolving over the subsequent 59 years. Today, the battlefield and our daily lives are littered with electronic devices that do everything from helping us to see in the dark to enabling global communication links. The transistors that act at the foundation of these capabilities are able to perform faster and faster every "Moore cycle". As the demand for faster processing in smaller electronics packages has grown, electronics makers have turned to a class of transistor called the Heterojunction Bipolar Transistor (HBT).

HBTs are transistors in which at least one of the two transistor interfaces is formed of two distinct materials [1]. The primary advantage of HBTs is their greater emitter efficiency, defined as the ratio of current injected into the emitter from an external source to the leakage current from the base to the emitter under active operation. This advantage results directly from the valence band discontinuity at the emitter-base heterojunction. The larger barrier to minority carrier injection from base to emitter allows for a substantial increase in the permissible doping level of the base layer of the HBT, which reduces sheet resistance and allows for thinner base layers without concern of emitter-collector leakage in the cutoff mode of operation. These advantages result in a faster base transit time, defined as the time required for the emitter injected carriers (minority

carriers in the base) to diffuse across the base layer to the collector, and a faster switching speed for the HBT. A schematic and energy band diagram is shown in Figure 1 highlighting the valence and conduction band discontinuities.

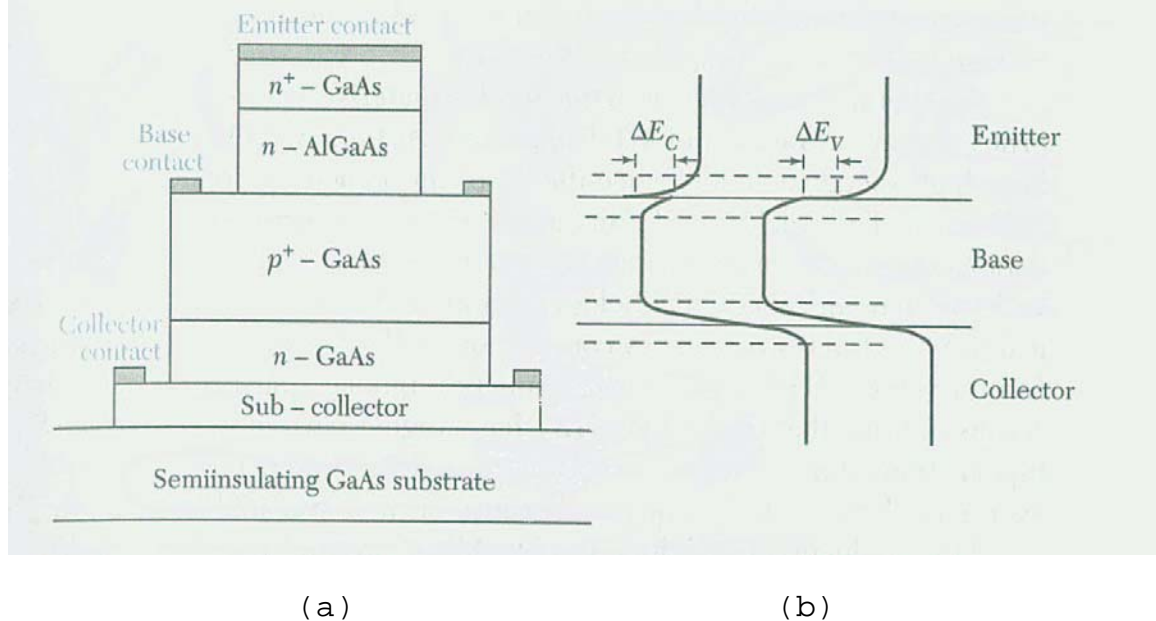


Figure 1. (a) Schematic cross section of an HBT structure.
 (b) Energy band diagram of a HBT operated under active mode. (From Ref.[1])

The use of different materials to provide these junctions, while adding complexity to the design, adds significant power amplification benefits and switching speed advantages [3]. Figure 2 shows a history of progression of highest cutoff frequency (F_T) for various transistors over time. The cutoff frequency is defined as the frequency where current gain of one is achieved. It is noted that the maximum working frequency of these devices, F_{\max} , is the frequency where power gain becomes unity and is below F_T [4].

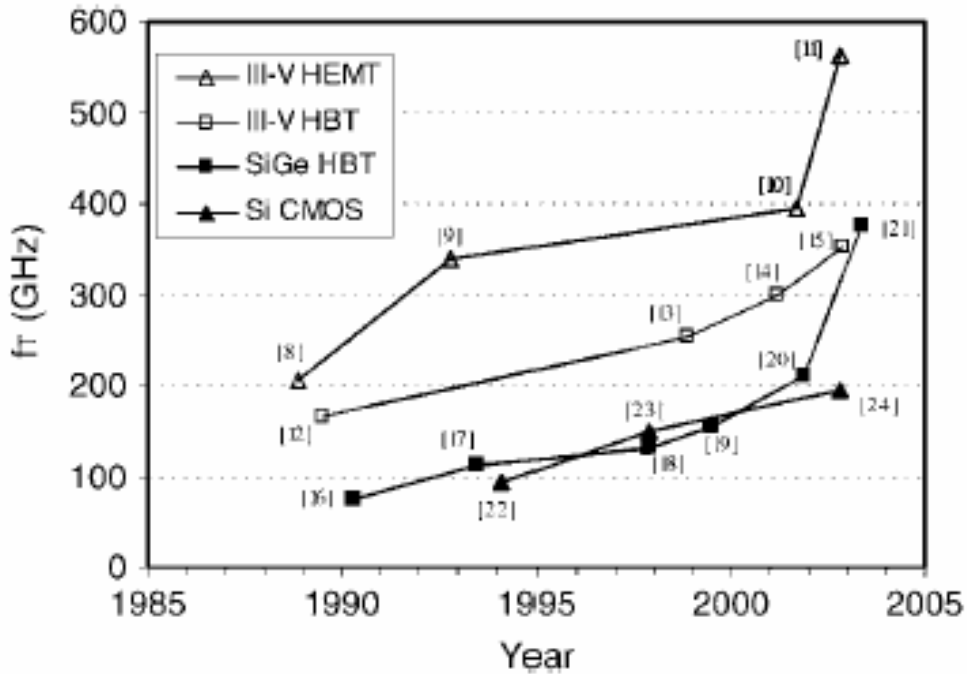


Figure 2. Trend of best achieved F_r for various transistors. (From Ref[4])

In order to achieve these frequencies of operation, manufacturers increasingly rely upon thinner, more heavily doped materials to propagate charge quickly and efficiently across the base to activate the transistor [1],[2],[5]. These increases in doping level and the shrinking of relative dimensions, in particular of the base layer, have coupled to bring about new and interesting regimes that operate on the edge of known macroscopically determined semiconductor transport properties. In order to effectively design and build the most efficient devices in these new highly doped low dimensional regimes, new techniques that can extract and model material properties on the sub-micrometer scale will be necessary [9].

B. MILITARY RELEVANCE

High speed electronics are important for a variety of military applications. The Terahertz frequency band, defined as the frequency range between 300 GHZ and three terahertz, is being explored for applications in medical diagnostic imaging, security imaging, and high bandwidth communications, just to name a few. A quote from a recent Defense Advanced Research Projects Agency (DARPA) Broad Agency Announcement (BAA) highlights what might be considered the most critical of these applications for our information centric battlespace.

The continuing need by DoD for ultra-high bandwidth communications and sensing will require electronics that operate at THz frequencies. Given that advanced microwave satellite communication systems already operate near 60 GHz, the instantaneous bandwidth required to fully monitor the battlespace will certainly exceed 300 GHz early in the next century. All communication bottlenecks must be removed so that surveillance systems can relay their wideband measurements to other locations for real-time analysis [10].

Conventional electronic sources and receivers are limited by resistances, capacitances, and transit times, resulting in a significant attenuation of high frequency power. High power amplifiers based on HBTs are beginning to approach the realm of terahertz oscillations and may provide a simple semiconductor based solution for an integrated coherent terahertz source and detector. A greater understanding of the physics of electrical carrier transport in these highly doped, low dimensional structures will aid the development of these devices and provide

manufacturers with more accurate models and predictive design tools.

C. THESIS OVERVIEW

In this thesis, (sponsored by National Science Foundation DMR 0203397) an application of a new technique for imaging charge transport is discussed [6-8]. A study of a series of low dimensional, heavily doped AlGaAs/GaAs heterostructures was conducted with an emphasis on the determination of the diffusion length of the minority carriers as a function of impurity doping. These results showed values of the minority carrier mobility that can only be explained with the incorporation of quantum mechanical scattering behavior at very high carrier concentrations. This appears to be the first direct measurement of diffusion lengths and minority carrier mobilities in this important material system [9]. Chapter II develops the mathematical model underpinning the transport of minority carriers in the low dimensional structures of interest. Chapter III briefly describes the experimental apparatus and the technique used to extract the material properties, while Chapter IV explores the theoretical limits of the model and demonstrates experimental evidence of those limits. In Chapter V the experimental evidence showing an increase in minority carrier mobility in heavily doped GaAs $\approx 10^{20} (cm^{-3})$ is presented, and the results are discussed in the context of existing theoretical work.

THIS PAGE INTENTIONALLY LEFT BLANK

II. TRANSPORT IMAGING IN THE TWO DIMENSIONAL LIMIT

A. OVERVIEW

SEM charge transport imaging combines two microscopes - a scanning electron microscope (SEM) to provide high resolution charge generation and an optical microscope to image the transport of charge. It can be performed in any material with a luminescent signature associated with charge recombination. In its basic operation, non-equilibrium minority carriers are injected into the luminescent semiconductor material by the SEM and the resulting radiative recombination is imaged through the optical microscope (OM). Analysis of the captured image allows quantitative, localized transport measurements.

One application for this technique is as a means to perform contact-free measurements of minority carrier diffusion lengths. This is a key parameter for many devices, including solar cells, photoconductors, and HBTs, as discussed in Chapter I. More conventional techniques for measuring diffusion lengths are generally limited by the need for contacts and the spatial averaging that occurs in macroscopic electrical measurements. Transport imaging can determine this important materials parameter directly from a single, zero bias luminescent spot image, particularly for samples in the 2D (thin layer) limit.

B. MODELING LIMITATIONS AND ASSUMPTIONS

In specific application to the materials of interest from Chapter I we consider the case where a thin sample is doped and the charge generation rate is sufficiently low so that we are able to model the transport of minority

carriers in an approximately constant distribution of majority carriers. For example, in doped samples of a $1\text{ }\mu\text{m}$ active layer AlGaAs/GaAs heterostructure, with incident electrons of ~ 15 keV, this means an electron beam current of $\sim 1\times 10^{-8}$ A or less for material doped at $\sim 1\times 10^{18}\text{ cm}^{-3}$. This approximation is made by assuming a highest value generation rate G of $G \sim E_{\text{acc}}/E_i$, where E_{acc} is the incident electron energy and E_i is the energy required to produce an electron/hole pair. For energies in the $\sim 5 - 40$ keV range, one can approximate $E_i \sim 3E_g$ for a bandgap of E_g [12]. The total carrier population $\Delta n \sim \Delta p$ created then per electron is $G\tau$. We approximate here a lifetime of $\tau \sim 1$ ns and a probe current of 1 nA, but the results can be scaled accordingly. In this example our ratio of resident majority carriers to minority carriers is on the order of 100. Therefore, our low injection limit is valid. The generation volume radius for the electrons was approximated from the model of Kanaya-Okayama as $\sim 1.5\text{ }\mu\text{m}$ in GaAs at 30 keV, with a hemispherical generation volume [13]. For more heavily doped materials, or shorter lifetime materials, one could use higher probe currents. Transport imaging can be performed outside these limits with more sophisticated modeling, but we will restrict ourselves to the low injection case for the analysis that follows.

C. MATHEMATICAL MODEL DEVELOPMENT

For cases where the diffusion length is comparable to or greater than our system resolution, diffusion of the minority carriers will broaden the luminescent spot. The extent of optical emission then becomes a function of minority carrier diffusion length and the diffusion length

can be directly extracted from the optical emission image. This approach cannot be easily applied to bulk/thick samples due to the generation volume created by incident electrons and the relatively weak dependence of the minority carrier distribution on diffusion length in 3D. However, since many new materials and devices utilize primarily thin films, (eg, heterostructures, quantum wells and specifically the base regions of HBTs) the range of applications for contact-free diffusion length measurements is large.

In order to extract the diffusion length from the optical image, we model a steady state distribution of minority carriers created by a generation region of finite extent. The SEM beam, operated in a low injection configuration, is the source of the generation region, and our 2D assumption is based upon the relatively thin depth of the active region compared with its extent in the other two dimensions.

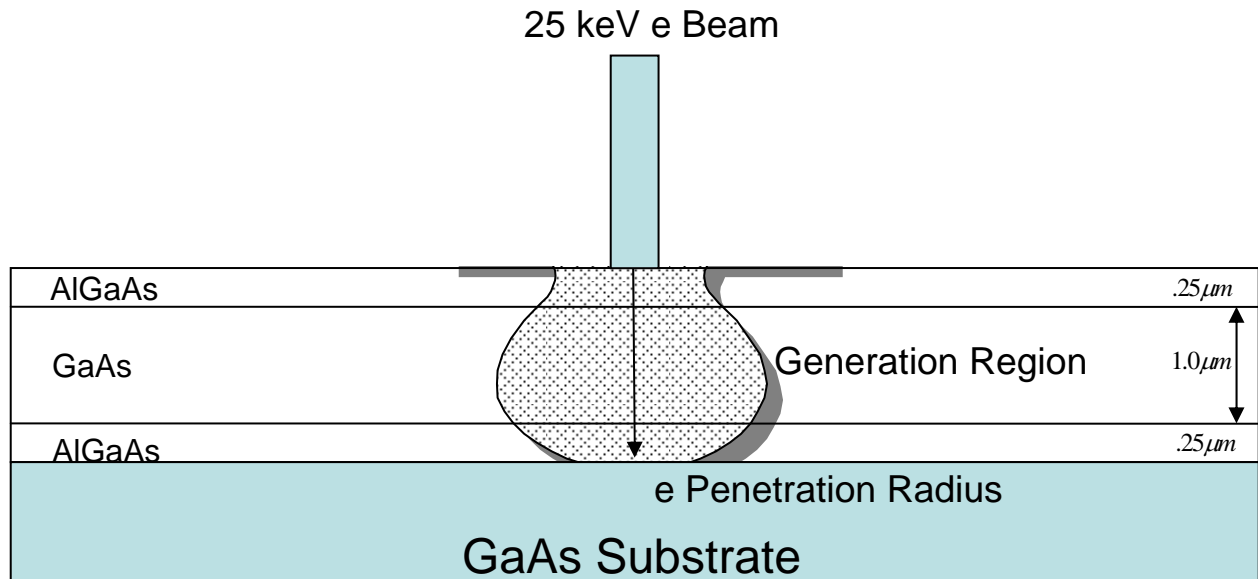


Figure 3. E-Beam/Sample interaction schematic

The sample reaches steady state very quickly, and we will describe the distribution of the minority carriers in the optically active GaAs layer. The heterostructure has been modulation doped with Be (p-type), and the minority carriers are electrons.

Beginning with the continuity equation for electrons in a p-type material:

$$(1) \quad \frac{dn}{dt} = G_n - U_n + \frac{1}{q} \vec{\nabla} \cdot \vec{J}_n$$

where G_n is the generation rate [$\text{1}/\text{cm}^3\text{s}$].

U_n is the recombination rate = $\frac{\Delta n}{\tau_n}$ for low injection.

$\frac{dn}{dt}$ is the time rate of change of electrons per volume per second.

\vec{J}_n is the current density vector

Δn is the number of excess minority carriers available for recombination

τ_n is the lifetime for electrons

Defining the steady state current density for carriers:

$$(2) \quad \vec{J}_n = q\mu_n n \vec{E} + qD_n \vec{\nabla} n \quad [\frac{C}{\text{cm}^2\text{s}}]$$

μ_n is the mobility of electrons in GaAs and

\vec{E} is the externally applied electric field.

D_n is the diffusion coefficient for electrons further related to the Diffusion Length by:

$$(3) \quad L = \sqrt{D_n \tau_n}$$

By combining the equations above we get:

$$(4) \quad \frac{dn}{dt} = G_n - \frac{n}{\tau_n} + \vec{\nabla} \cdot \left[\mu_n n \vec{E} - \frac{L^2}{\tau_n} \vec{\nabla} n \right]$$

By our assumption we are at steady state and therefore the time rate of change of the electron distribution is zero. Now, assume a constant E field in the x direction so that $\vec{E} = qE\vec{x}$, and Equation (4) becomes:

$$(4.5) \quad 0 = G_n - \frac{n}{\tau_n} + \mu_n E \frac{dn}{dx} + \frac{L^2}{\tau_n} \vec{\nabla}^2 n$$

By multiplying through by $\frac{\tau_n}{L^2}$ and making the substitution: $S = \mu\tau E$, where S is the drift length, we get Equation (5).

$$(5) \quad \vec{\nabla}^2 n + \frac{S}{L^2} n_x - \frac{1}{L^2} n = \frac{-G_n \tau_n}{L^2}$$

1. Generation Region

Here we make a digression to discuss the nature of $G_n \tau_n$, the steady state generation distribution created by the balance between the continuous SEM injection and recombination within the sample. After Donolato and Venturi we can define the distribution as a depth dosed Gaussian distribution [15].

$$(6) \quad g(r, z; R) = \frac{g_o}{R} \frac{\Lambda\left(\frac{z}{R}\right)}{2\pi\sigma^2(z, R)} e^{\frac{-r^2}{2\sigma^2(z, R)}}$$

Here the key feature of the distribution is the variance σ being formed of two linearly independent factors:

$$(7) \quad \sigma^2(z, R) = \sigma_o^2 + \sigma_s^2(z, R)$$

where σ_o is the variance of the beam and σ_s is the spread of the primary and secondary electrons in the sample due to scattering. z and R are the depth coordinate and the primary electron range respectively. R is a function of beam energy and the atomic number and density of the target material.

Let σ_o be the measure of the diameter of the circle within the beam that contains 50% of the total beam current, or $d=\text{beam diameter}=1.67\sigma_o$. From empirical measurements we can assume that the lateral scattering variance $\sigma_s \approx 0.1 \frac{z^3}{R}$ [15]. R can be determined from ref [16] for a beam energy of 15keV in GaAs to be approximately $\approx 1.5\mu m$, and $\approx 2.0\mu m$ for a 25 keV beam energy. Though there is variation in the generation shape as shown in Figure 3 as a function of the depth (z) we approximate the variance as constant for the generation region in our active layer. Assuming an average depth of $R/2$ the generation variance becomes:

$$(8) \quad \sigma(z, R) = \sqrt{.36d^2 + 0.1\left(\frac{R}{2}\right)^2}$$

For a 15 keV beam energy and $d=1.75\mu m$, $\sigma_{gen} = 1.06\mu m$, and the radius within which 99% of the charge will be generated

is $2\sqrt{2}\sigma = 3\mu m$. This 99% value will define the limits of our source region for numerical integration in later sections.

We define our generation function for the source term and normalize the output to 1 using Equation (6):

$$(9) \quad g(r') = e^{\frac{-r'^2}{2\sigma^2}}$$

2. Green's Function Solution

Returning to the differential Equation (5) with the inclusion of the source function, Equation (9):

$$(10) \quad \bar{\nabla}^2 n + \frac{S}{L^2} n_x - \frac{1}{L^2} n = \frac{-1}{L^2} e^{\frac{-r'^2}{2\sigma^2}}$$

By the use of an integration factor we can conduct a change of variables to eliminate the n_x term thereby making Equation (10) into the Helmholtz equation. Substituting:

(11) $n(x, y) = w(x, y)e^{ax}$ into (10) and combining terms we get:

$$(12) \quad e^{ax} \left(w_{xx} + w_{yy} + 2aw_x + a^2 w \right) + \frac{S}{L^2} e^{ax} (w_x + aw) - \frac{1}{L^2} e^{ax} w = \frac{-1}{L^2} e^{\frac{-r'^2}{2\sigma^2}}$$

Combining like terms and dividing through by the exponential:

$$w_{xx} + w_{yy} + w_x \left(2a + \frac{S}{L^2} \right) + w \left(a^2 + \frac{Sa}{L^2} - \frac{1}{L^2} \right) = \frac{-1}{L^2} e^{\frac{-r'^2}{2\sigma^2}} e^{-ax}$$

Now we choose $2a + \frac{S}{L^2} = 0$ or $a = -\frac{S}{2L^2}$ in order to eliminate the derivative term to obtain:

$$(13) \quad w_{xx} + w_{yy} - \frac{S^2 + 4L^2}{4L^4} w = \frac{-1}{L^2} e^{\frac{Sx}{2L^2}} e^{\frac{-r'^2}{2\sigma^2}}$$

which is nothing more than the Helmholtz equation where the Helmholtz operator is : $\nabla^2 + K^2$ and $K = i \frac{\sqrt{S^2 + 4L^2}}{2L}$.

Recognizing that the Green's Function for the Helmholtz operator is the zeroth order Bessel Function of the second kind [16],

$$(14) \quad G(r; r') = \frac{1}{2\pi} K_0 \left(k |r - r'| \right)$$

where k is the real part of K : $k = \frac{\sqrt{S^2 + 4L^2}}{2L}$.

The general solution to a Green's Function problem is

$$w(x, y) = \int_0^\infty G(r; r') \frac{1}{L^2} e^{\frac{Sx'}{2L^2}} e^{-\frac{r'^2}{2\sigma^2}} dr'$$

Returning to the solution for the electron distribution (n)

by the substitution: $n(x, y) = w(x, y) e^{ax}$ or $n(x, y) = w(x, y) e^{\frac{-S}{2L^2}x}$

Now,

$$(15) \quad n(x, y) = \frac{1}{2\pi} \frac{1}{L^2} \int_0^\infty K_0 \left(\frac{\sqrt{S^2 + 4L^2}}{2L} |r - r'| \right) e^{\frac{Sx'}{2L^2}} e^{-\frac{Sx}{2L^2}} e^{-\frac{r'^2}{2\sigma^2}} dr'$$

By defining our limits of integration equal to the radius which contains 99% of the generation region's minority carriers as described by the Gaussian distribution in Equation (8) our model for the minority carrier distribution including diffusion and drift in 2D becomes:

$$(16) \quad n(x, y) = \frac{1}{2\pi L^2} \int_0^{2\sqrt{2}\sigma} K_0 \left(\frac{\sqrt{S^2 + 4L^2}}{2L} |r - r'| \right) e^{\frac{S(x' - x)}{2L^2}} e^{-\frac{r'^2}{2\sigma^2}} dr'$$

The algorithm in Appendix A.5 is a Matlab coded version of this solution using a double quadrature numerical

integration scheme to calculate the distribution of carriers as they drift/diffuse from the finite area defined by the Gaussian generation function (9) and bounded by the circle of radius $2\sqrt{2}\sigma$.

THIS PAGE INTENTIONALLY LEFT BLANK

III. EXPERIMENTAL APPARATUS

A. INTRODUCTION

The minority carrier distribution in a semiconductor sample reveals information regarding the transport properties of the material itself. As shown in the previous chapter the diffusion length of the minority carriers determines the shape of that distribution. The novelty of the Transport Imaging technique is the extraction of the salient aspects of that distribution from an actual sample in a controlled and flexible manner. By combining the charge injection and high resolution electron imaging capabilities of a Scanning Electron Microscope (SEM) with the optical resolution of a Silicon Charge Coupled Device (CCD) Camera, accurate spatial representations of these distributions are captured and analyzed. A custom software solution allows for the analysis of these images and the fitting of the experimental data to the mathematical model's predictions.

B. APPARATUS DESCRIPTION

The charge transport imaging instrument combines two independent microscopes - a JEOL SEM (See Table 1 for instrument specifications) for generating charge and an optical microscope (OM) for collecting and imaging the luminescence emitted from the recombination process. Using a retractable arm, the OM is placed directly under the pole piece in the SEM, allowing the electron beam to pass through the center of the first optical collecting surface. The initial demonstration system modifies an OM attachment for the JEOL SEM that was originally designed to allow the

fine adjustment of sample height required for wavelength dispersive X-ray spectroscopy (WDS). WDS provides higher energy resolution than traditional energy dispersive X-ray analysis (EDX) and requires sensitive control of sample height in order to maintain proper conditions for multiple diffraction angles. OMs designed for this purpose have short focal lengths and are normally used in conjunction with a lamp source and low sensitivity near-IR/visible imager.

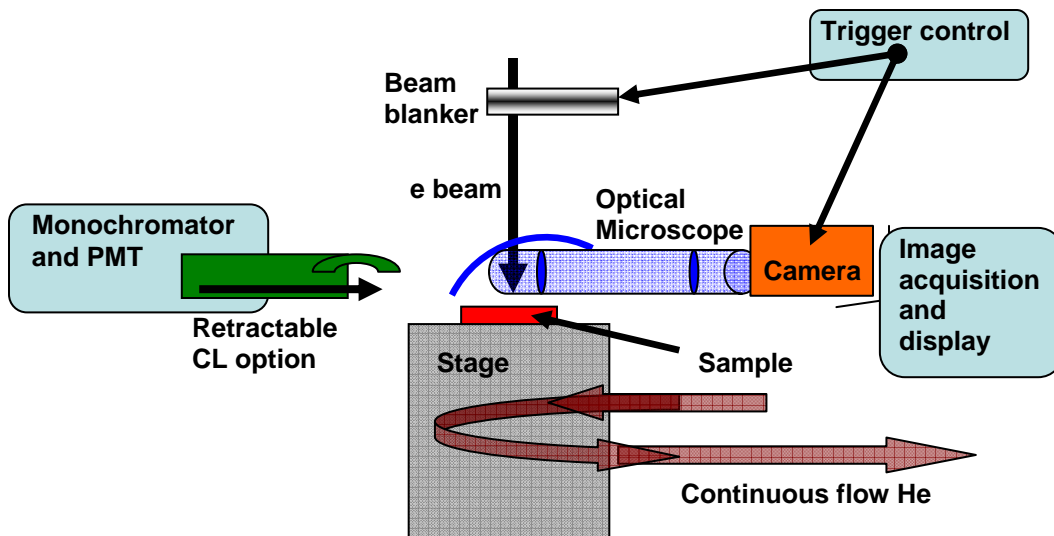


Figure 4. Transport Imaging System Schematic

A schematic of the system is shown in Figure 4. In addition to the charge transport imaging microscope, the instrument is equipped with standard CL capability using a Gatan (formerly Oxford Instruments) system with a parabolic mirror, $\frac{1}{4}$ m monochromator and TE cooled GaAs PMT as the detector. Beam blanking capability exists for future time resolved work. Finally, the instrument has a liquid helium cooled stage, so that transport imaging and conventional CL can be performed over a temperature range from 300 to \sim 5 K. The system uses continuous flow liquid He, with the

sample stage inside the SEM mounted in a cold finger configuration.

Variable accelerating voltage; 200 to 40,000V
Variable probe current; 1x10E-8 to 1x10E-12 Amps
Maximum sample size of 6" in any one dimension
Working distances; 8 to 48mm
Sample rotation; 360°
Sample tilting 90°
Variable magnification; 10x to 300,000x
Maximum resolution; 10 nm
Secondary and Backscattered Electron detectors
Equipped with EDS capable of detecting Carbon and forming X-ray maps of composition; composition to within 0.1 wt%
Integrated digital imaging system
Noise reduction through frame averaging
Image capture and export in electronic form (TIFF)
Low cost, medium quality thermal printouts
High quality, medium cost Polaroid type 55 film containing both negative and positive

Table 1. JEOL 840A Specifications (From [11])

For transport imaging, the OM is used in a passive detection mode, detecting light emitted directly from the sample using a high sensitivity cooled Si CCD array camera. The current camera uses a 2184 x 1472 pixel array (15 mm x 10 mm), with a pixel size of 6.8 x 6.8 μm^2 and can be used for transport imaging for wavelengths from ~ 350 to 1100 nm. Initial image processing is performed using MicroCCD, a software program provided with the CCD camera. Although further image and data processing are often required for individual investigations, we benefit from excellent existing image acquisition and processing capabilities, often developed to support astronomical communities using similar cameras for low light imaging.

The optical microscope insert is a basic two lens system (objective and eyepiece) modified to allow for passage of an incident electron beam. The considerations, as with any optical microscope, are resolution and magnification. Estimating the resolution for incoherent emission as

$$(17) \quad \Delta y \sim \frac{0.61\lambda}{NA}$$

(where Δy is the spatial resolution, λ is the wavelength and NA is the numerical aperture (set here at 0.95 max)), we find $\Delta y = 0.56 \mu\text{m}$ for $\lambda = 870 \text{ nm}$ (e.g., room temperature emission from GaAs) and $\Delta y = 0.22 \mu\text{m}$ for $\lambda = 350 \text{ nm}$ (e.g., emission from GaN). The current magnification of the optical system is $\sim 20x$, i.e., a $5 \times 5 \mu\text{m}^2$ area scanned by the e beam creates a $100 \times 100 \mu\text{m}^2$ area on the CCD area. As mentioned, pixel dimensions are $6.8 \mu\text{m}$, so the resultant effective scale for the final image is $\sim 0.4 \mu\text{m}/\text{pixel}$, comparable to the resolution limit for red/near IR light. In order to select photon emission from specific regions within the sample, appropriate combinations of bandpass filters are placed within the optical path for wavelength selection. The filters are used to eliminate, for example, substrate luminescence or to select the transport of interest in a multilayer sample.

While the optical resolution limit is the fundamental mechanical limit of the luminescence collection, there exists a further analytical bound on the extraction of transport properties related to the data extraction method.

C. DATA EXTRACTION

As discussed previously, the transport property information is contained in the distribution of minority carriers at steady state. This distribution is directly linked to the resulting photon distribution as captured in an image by our device. Figure 5 shows one such image.

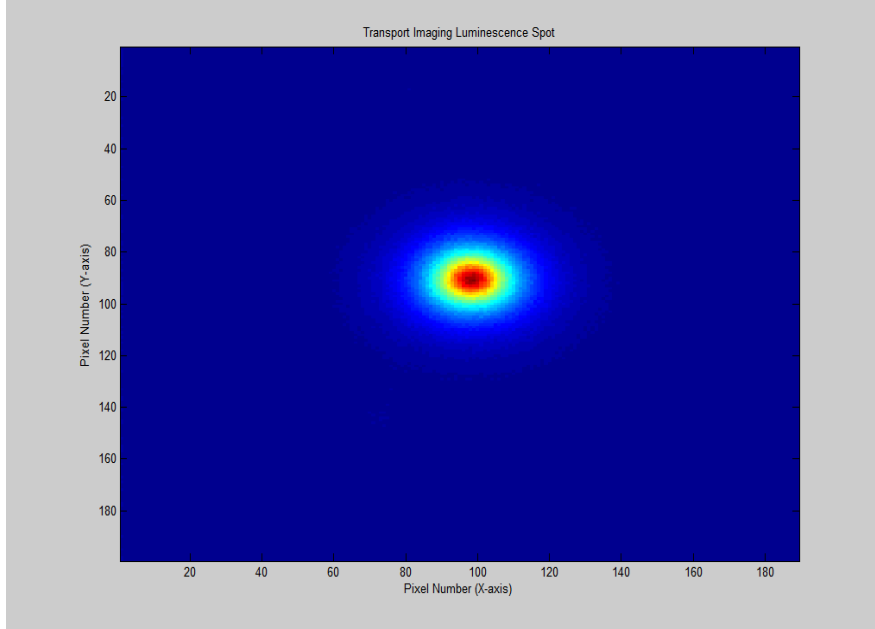


Figure 5. CCD image of Experimental Sample

The data underlying this image is a 2x2 matrix whose indices correspond to pixel number. The values entered in each element (0-10,000) of this matrix are the raw intensity of the photon emission collected by the CCD. In order to study the full extent of the distribution of minority carriers with greatest resolution, we extract line segments that cross the peak intensity point of the image. Though various methods may be employed to select these data sets, in this work that extraction was conducted via an algorithm written in MATLAB code (See appendix A.1- "imagedatamanipulator.m"). Once a line segment is extracted, it must be parameterized and fitted to the model

equation developed in Chapter II. This fitting can be accomplished via two methods with varying degrees of flexibility and resolution.

1. Slope Analysis Estimation

By assuming that the argument of the Bessel function is large compared with 1 we can assume the distribution approximates a negative exponential.

$$\text{With } r \gg L_d : K_o\left(\frac{r}{L_d}\right) \rightarrow e^{\frac{-r}{L_d}}$$

so that the slope of this line segment plotted on a semilog

$$\text{plot would be } m = \frac{-1}{L_d} = -\sqrt{\frac{e}{\mu \tau k T}} \text{ where}$$

m is the slope and $r = \sqrt{x^2 + y^2}$, and all other terms are as defined in Chapter II. Figure 6 shows a semilog plot of a line segment extracted from the image of Figure 5.

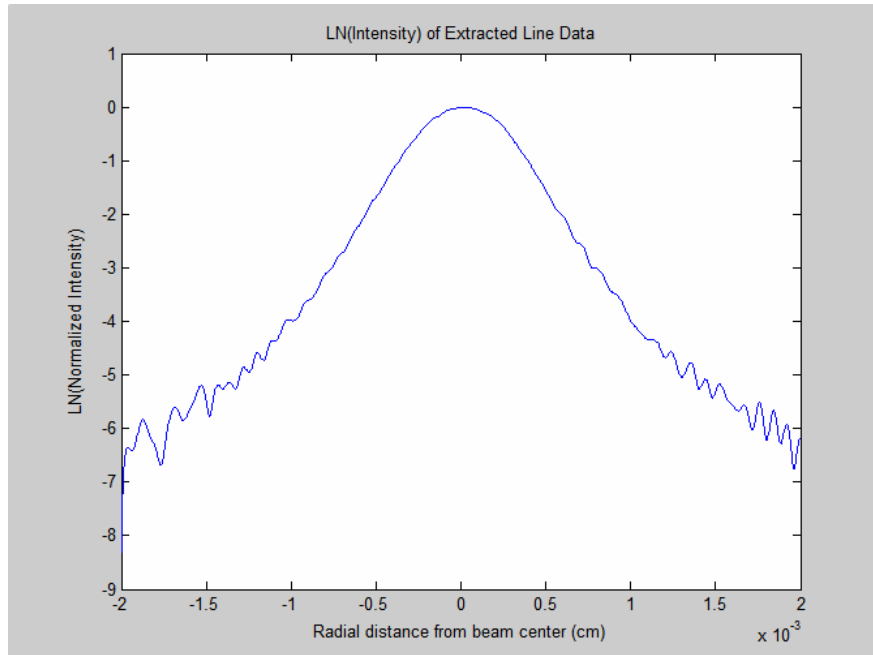


Figure 6. Semilog plot of extracted line of luminescence from Data Image of Figure 5.

Figure 7 shows the results of the slope analysis as calculated by the "Slope2.m" algorithm of Appendix A.3.

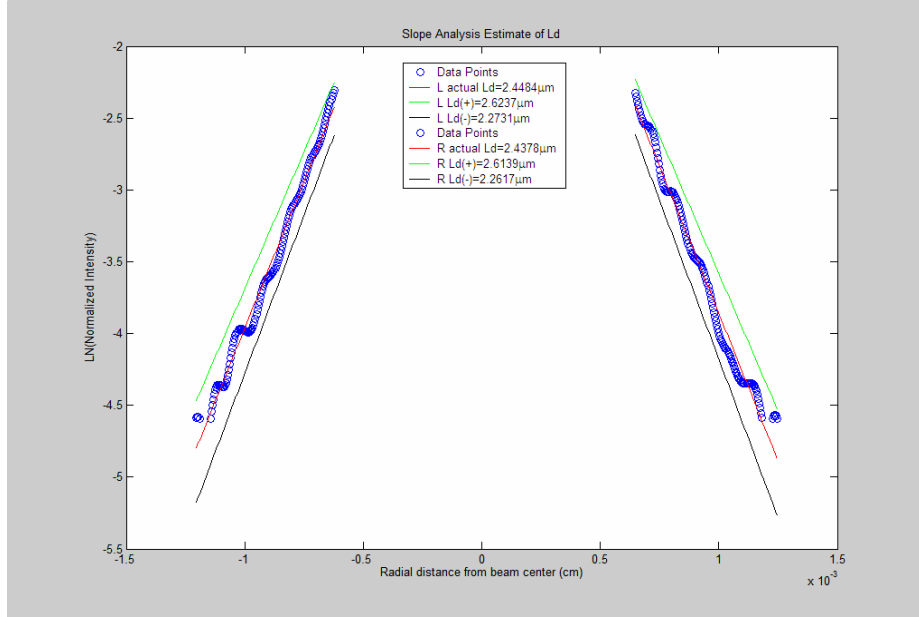


Figure 7. Slope Analysis for Experimental Sample

The error bars here are derived from the slope calculation of the distribution when the maximum possible mechanical error limits ($\pm 0.4 \mu\text{m}$) are assumed for the first and last points in the data sample. This error analysis is utilized instead of a standard deviation of data points from the linear regression due to its physical nature. It provides an intuitive link between the analytical assessment and the mechanical limits of our apparatus.

The benefits of the slope analysis technique lie in its direct extraction of transport properties from an image with limited fitting or data manipulation. Depending on signal to noise ratio and sample luminosity it can provide knowledge of a material's diffusion length over a roughly $3 \mu\text{m}^2$ area. This material property resolution is limited by the optical resolution of the system (pixel width) in the $\hat{\phi}$

direction, equal to $0.4\mu m$, and the number of pixels required to conduct the linear regression analysis in the \hat{r} direction. Figure 8 shows a pictorial of resolution dependence on data sample size and selection. The resolution listed in the figure follows from Figures 4-6.

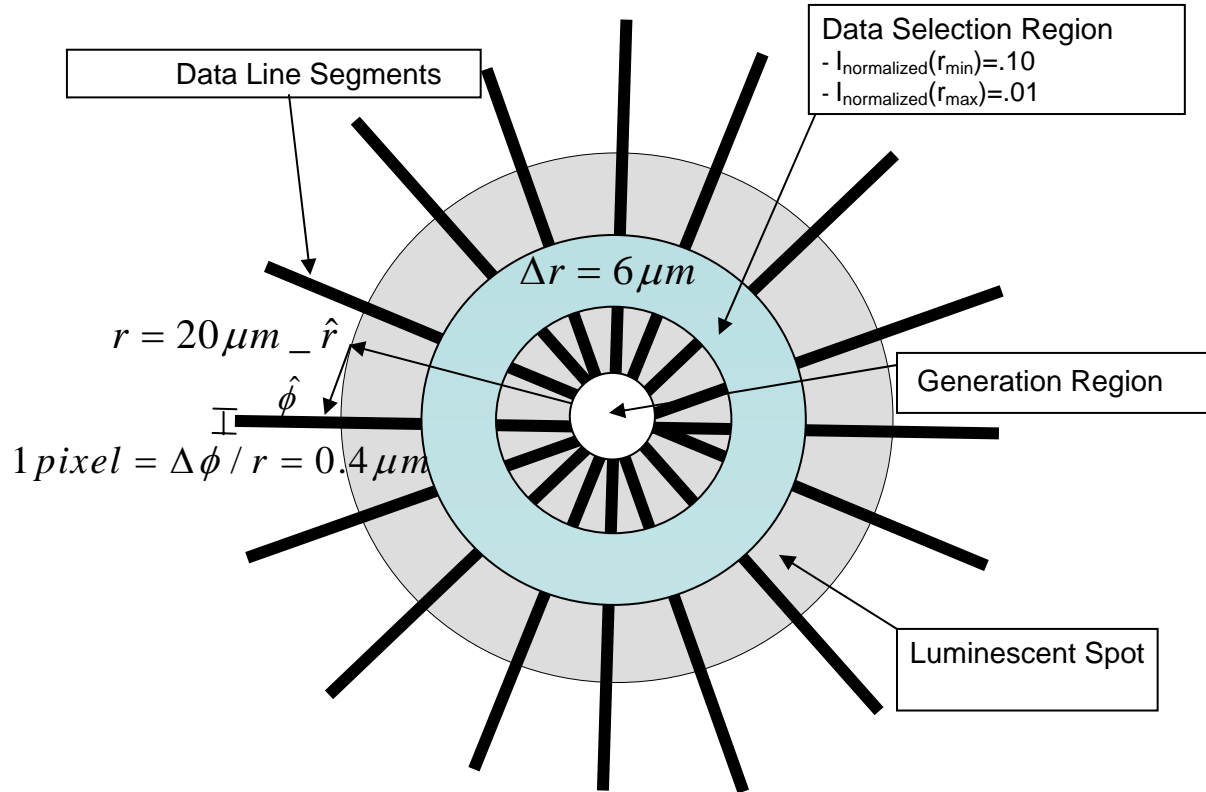


Figure 8. Slope Analysis resolution

So in this case, the sample resolution of transport properties is averaged over an area of $0.4\mu m \times 6\mu m$ or $2.4\mu m^2$.

As mentioned, the sample size and region selection is a function of the interplay between signal to noise ratio, error analysis and the large r limit. Lower error estimations require a larger number of data points, while for most samples, noise limitations drive our outer limit

below the ideal $r/L_d \gg 1$ limit. In work done by M. Talmadge of Fairfield University, Fairfield CT, it has been shown that when $r > 9L_d$ the extracted $-1/m$ is within 95% of the actual L_d . Figure 9 shows the trend of predicted L_d vs. actual L_d as a function of r/L_d [14].

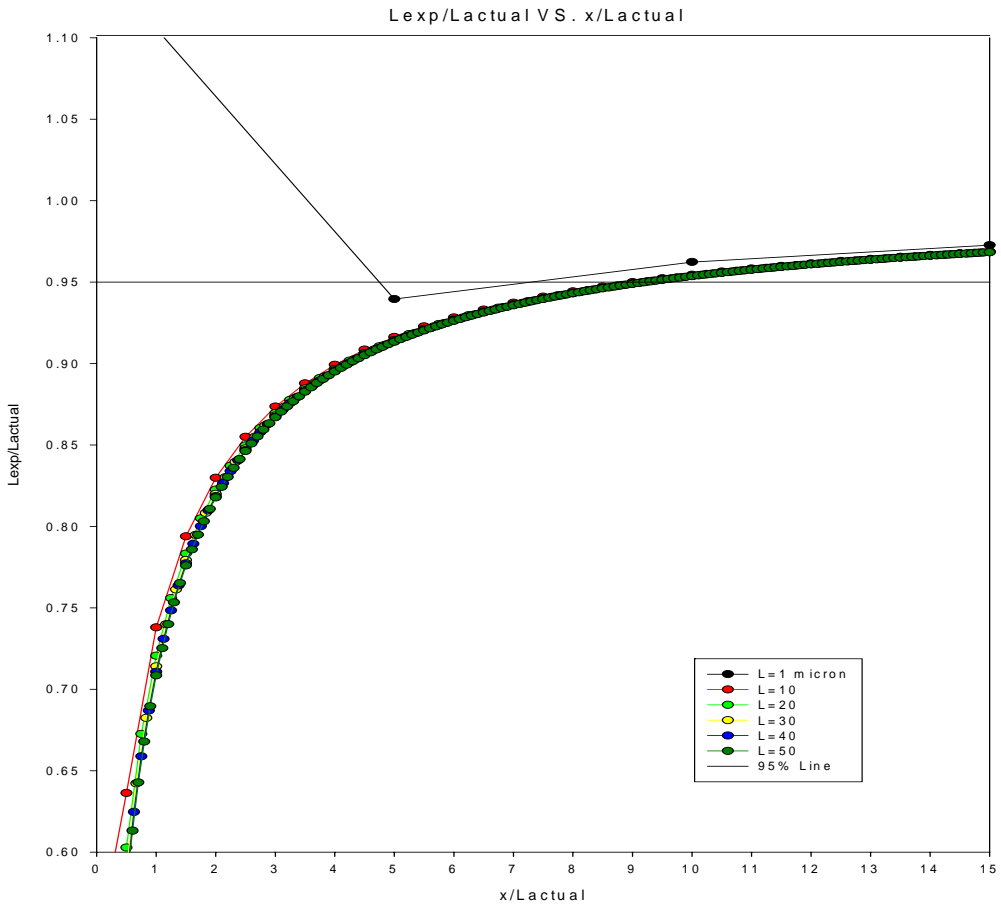


Figure 9. Slope Method Assumption Dependence on large Bessel Function argument

However, when L_d is not known it is more difficult to determine this confidence factor. Work is currently being done to perfect a second derivative analysis to determine this confidence factor without *a priori* knowledge of the actual L_d . Additionally, when our samples are of low luminosity and have short diffusion lengths the collected

photon emission does not possess the required extent to allow data selection within reasonable limits of $r/L_d \gg 1$. In this case a drift analysis is preferable however, it also possesses similar limitations.

2. Least Squares 2-Parameter Fit Analysis

By applying an iterative least squares analysis (See algorithm Appendix A.4) one can fit the model prediction from Equation (16) to the full distribution of the extracted line of data and determine the diffusion length of the minority carriers and the radius of 99% charge generation. This analysis technique provides an additional understanding of the generation region dimension and is unencumbered by the limitations of the $r/L_d \gg 1$ limit. However, it increases the area of the sample used to extract a diffusion length - effectively reducing the resolution of the technique from $\approx 3\mu m^2$ to as large as $\approx 16\mu m^2$ for the same sample data from Figure 5. An example of a completed fit is shown in Figure 10, where n is defined as the radius which encompasses 99% of the carrier generation or $n = 2\sqrt{2}\sigma$.

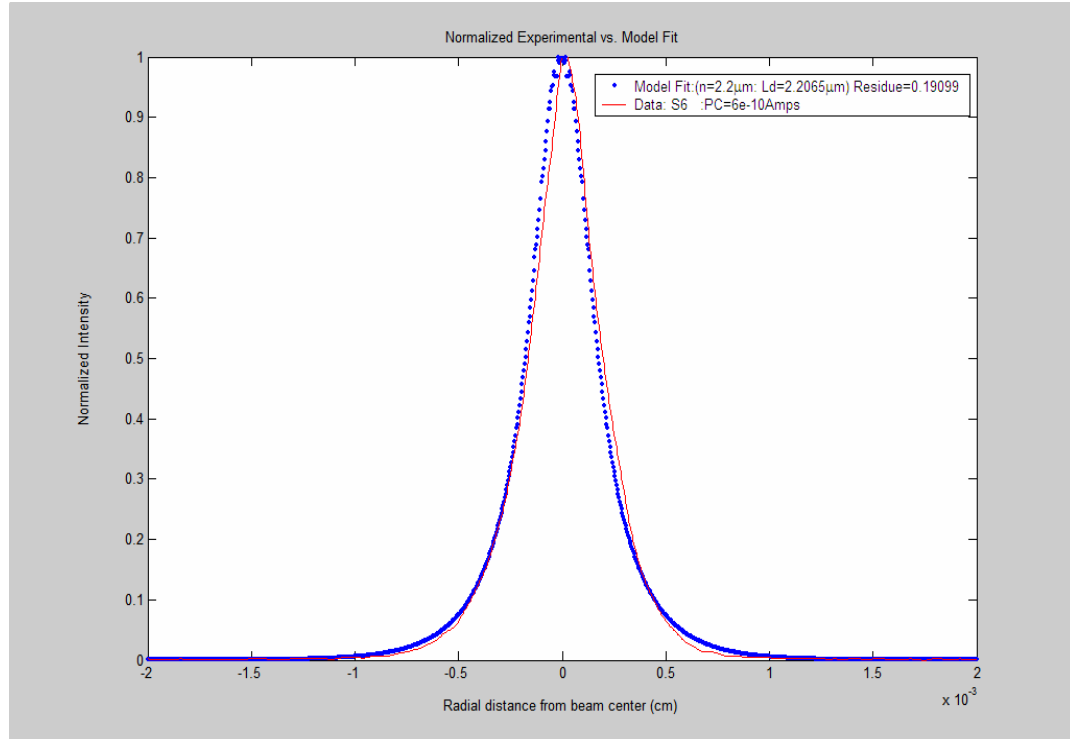


Figure 10. Least Squares Model Fit of Experimental Data

While the area over which the parameters are determined is larger, this technique benefits from the possibility of greater accuracy in determination of those parameters. Moreover, when the material studied has a diffusion length greater than our optical resolution, with appropriately taken data and reasonable signal to noise ratios we expect to extract diffusion lengths and generations region radii accurate to within $\pm 0.1 \mu m$. As mentioned before, this method is not limited by the necessity to take data far from the generation source, which is difficult for materials of low luminescence. However, there are inherent limits to the materials and conditions which can be treated with this analysis.

THIS PAGE INTENTIONALLY LEFT BLANK

IV. TRANSPORT IMAGING PREDICTIONS AND LIMITATIONS

A. ERROR ESTIMATION FOR CURVE FITTING ALGORITHM

Apart from noise and resolution limits, there are two primary sources of error in this technique; 1) the fit of the model data to the experimental data, and 2) the assumptions that underlie our mathematical model. We can treat the quality of the model fit through the calculation of a root mean square error (RMSE).

The residue listed in the legend in each figure is the sum of the least squares difference used to select the most appropriate parameter fit. From this residue one can calculate the RMSE of the fit, or

$$RMSE = \left(\frac{\phi}{M} \right)^{\frac{1}{2}}$$
 where $\phi = residue = \sum_{i=1}^{M=1000} (I_{pred} - I_{data})^2$ and M is the number of data points taken from the sample and used in the model calculation. This is a direct measure of the undetermined error of the fit to the distribution. Using this formulation we routinely achieve very favorable RMSEs ($\leq 10^{-2}$).

As was noted, our optical resolution is approximately $0.4\mu m$, which results in only 100 data points taken over the $40\mu m$ interval shown in the figure. In order to smooth the distribution, we use a spine interpolation technique to increase our data set by a factor of 10. For relatively well behaved distributions, which these are, this technique has been shown to not alter the predictions of the model, yet allows a much higher confidence in the curve fit.

Because the model distribution is generated by a numerical integration calculation of an integral expression and the parameters are themselves arguments of non-linear functions, it is not readily apparent how this RMSE correlates to error bars in the parameters themselves. This analysis can be done and is explained in many non-linear least squares fitting texts, but it is more physical to vary diffusion length and generation radius by a small amount and observe the resulting magnitude of the RMSE from our model fit. The next series of plots show this estimation.

In order to establish a base line algorithm precision we first produce a model output for parameter values $n = 3.0\mu m$; $L_d = 2.0\mu m$, then allow the least squares fitting routine to analyze that output and fit it with the appropriate parameters. When the integration step size is identical for the model produced output and the least squares fitting algorithm the residue is 0 as expected. This is shown in Figure 11.

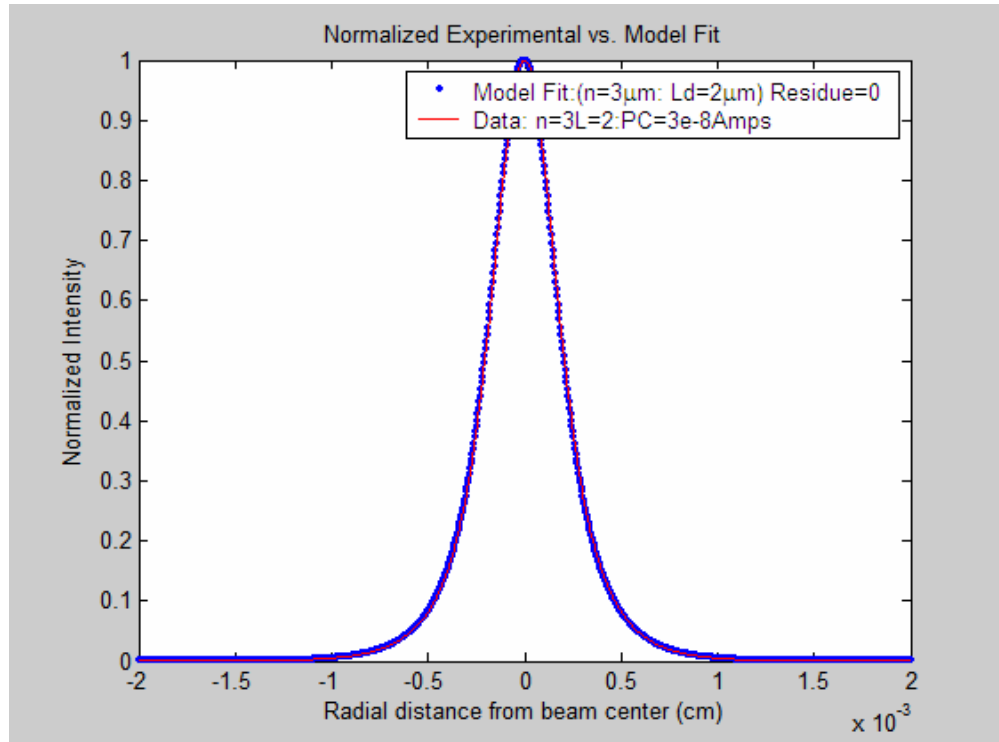


Figure 11. Baseline calculation error in Model Fit algorithm (no variation of integration step size)

A slightly more realistic assumption is that our numerical integration step size is on the order of 1000 times smaller than that of the experimentally captured distribution. Figure 12 shows the effect of a difference in integration step size of a factor of 1000 between the model produced curve and the least squares fitted curve.

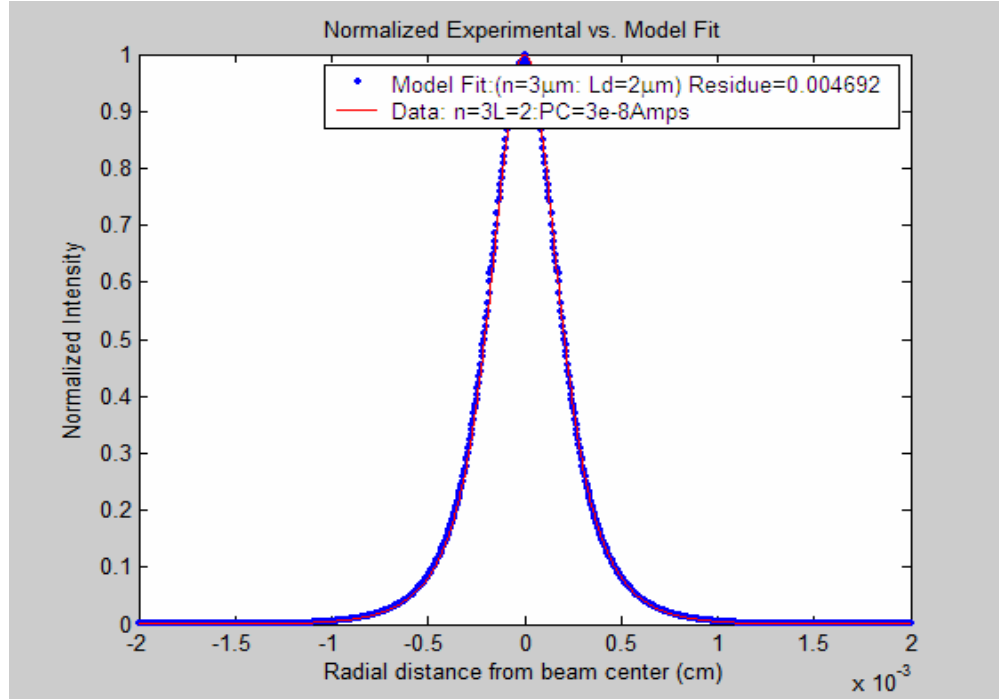


Figure 12. Baseline calculation error in Model Fit algorithm (variation of integration step)

The Residue of .004692 yields an RMSE of .0021 – an order of magnitude less than we typically see in our fitting to experimental data. We can, of course, reduce this step size but at the expense of integration time and given the very real effect of noise in our collected data, it is unrealistic to believe that we can achieve greater precision at room temperature through further reductions.

In order to see the effect of parameter errors on the Residue we again employ the algorithm to produce an ideal model distribution and fit it with our least squares routine. The figures that follow show forced errors in the model fit of the same ideal data set and the impact on the size of the residue. We vary diffusion length ($0.1\mu m$ and $0.2\mu m$) and generation region radius ($0.1\mu m$ and $0.01\mu m$) and calculate the RMSE in Table 2. It is noted that the RMSE

value is approximately the same for equal variations in either parameter.

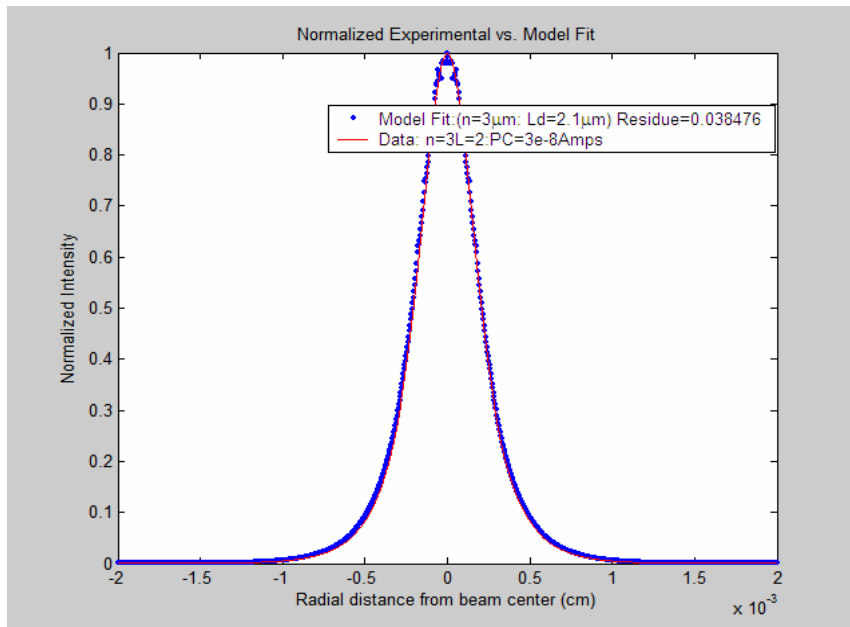


Figure 13. Error estimation for $0.1\mu\text{m}$ variation in Diffusion Length RMSE= 6.2×10^{-3}

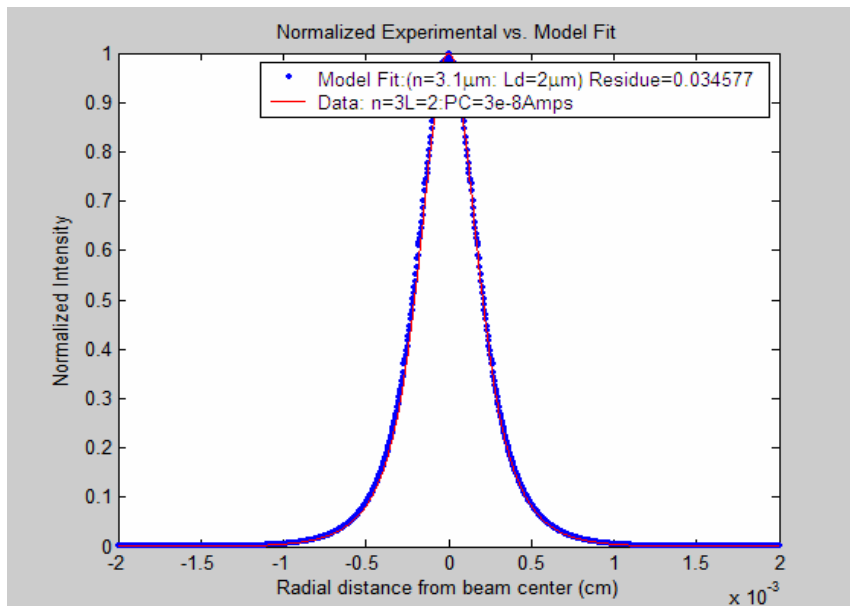


Figure 14. Error estimation for $0.1\mu\text{m}$ variation in Generation Region radius RMSE= 5.8×10^{-3}

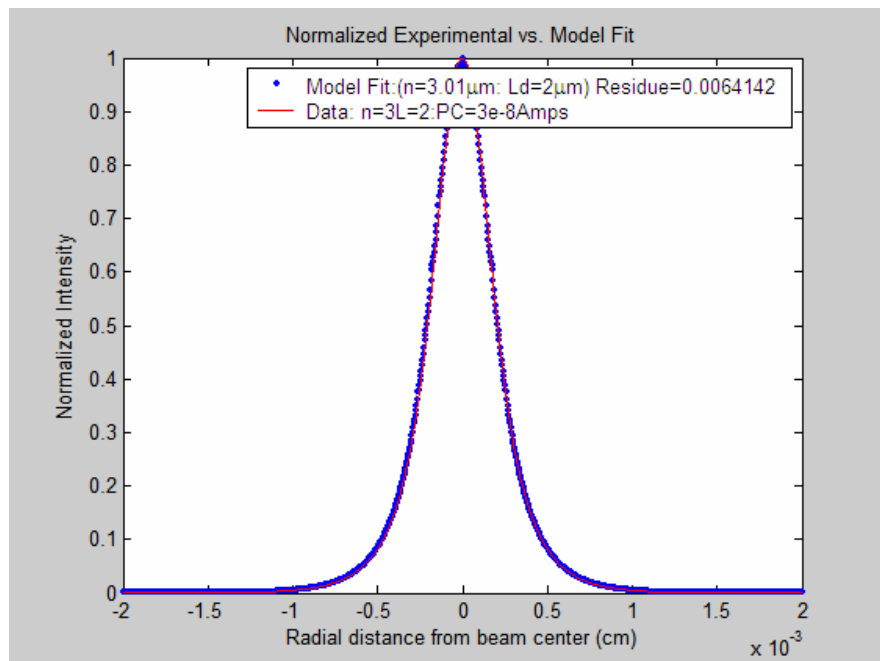


Figure 15. Error estimation for $0.01\mu m$ variation in Generation Region radius RMSE= 2.5×10^{-3}

Another reference point for observed errors is shown in Figure 16.

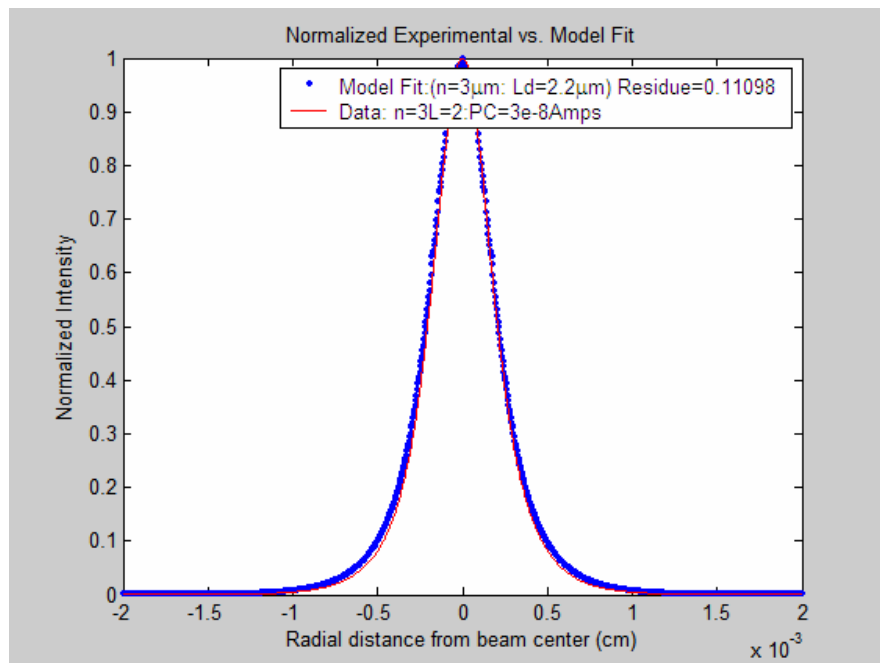


Figure 16. Error estimation for $0.2\mu m$ variation in Generation Region radius RMSE= 10.5×10^{-3}

<u>Residue</u>	<u>RMSE</u>	<u>L or n Variation</u>
.0064	2.5×10^{-3}	$\pm 0.01 \mu m$
.0384	6.2×10^{-3}	$\pm 0.1 \mu m$
.1110	10.5×10^{-3}	$\pm 0.2 \mu m$
.4763	21.8×10^{-3}	$\pm 0.5 \mu m$
1.6853	41.1×10^{-3}	$\pm 1.0 \mu m$

Table 2. Tabulated Error Estimates for Curve Fits

B. LIMITS OF MODEL ASSUMPTIONS

A more fundamental error resides in the boundaries of where our model assumptions break down, or where other aspects of transport begin to play a more dominant role. There is much interesting science in this aspect of the analysis, and in fact, Chapter V will focus on the interplay of one such phenomenon, photon recycling, which at high doping levels begins to affect the luminescence distribution on a scale that demands special treatment.

1. Low Injection Assumption

An important limitation in our modeling is our assumption of low injection. As described in Chapter II.B. for these samples we are restricted to probe currents equal to or below $1 \times 10^{-8} A$. Above this level of excitation we significantly alter the distribution of majority carriers in the vicinity of the generation region and the recombination is no longer appropriately described as proportional to the density of minority carriers alone. In order to probe this limit and to compare the slope analysis predictions with the model fit technique, we will observe a

series of data taken from the same spatial location on an AlGaAs/GaAs heterostructure kept at a temperature of 4.7 K, and constant beam energy of 25 keV while the probe current was varied from $6 \times 10^{-12} - 6 \times 10^{-8} A$. Previous work within our lab has reported the effect of increasing SEM probe current on the size of the luminescent spot [17]. Here a series of images is presented corroborating this work and quantifying the increase in the standard deviation of the generation distribution. Figure 17 shows a schematic of the heterostructure as designed by Tom Boone at Hitachi Labs.

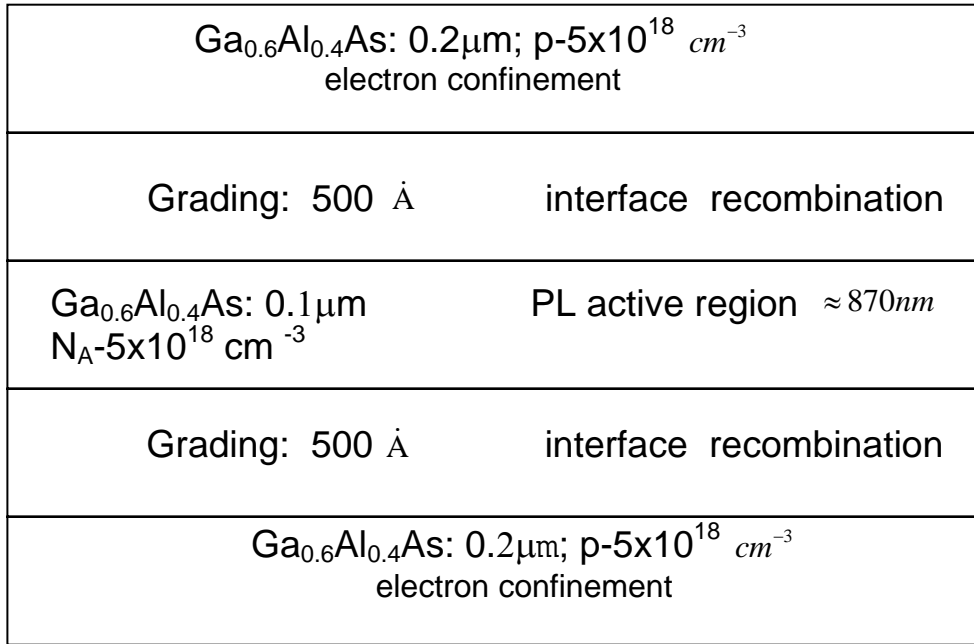


Figure 17. AlGaAs/GaAs Heterostructure design from Tom Boone Doctoral Dissertation [22]

The study of these materials at low temperatures allows a greater signal to noise ratio, which enables greater accuracy of the model fit. Previous work in our lab has shown that the minority carrier diffusion length in these materials is independent of sample temperature, and therefore we can use these measurements to establish a

baseline of accuracy between the two techniques that should translate to higher temperatures [23]. Table 3 compiles the salient results from the analysis of this sample at 4.7 K.

Probe Current	L_d by Slope Analysis (μm)	L_d by Model Fit (μm)	$2\sqrt{2}\sigma$ Generation Region	RMSE of Model Fit
$6 \times 10^{-12} \text{ A}$	10 ± 8	3.9 ± 0.5	3.2 ± 0.5	25×10^{-3}
$6 \times 10^{-11} \text{ A}$	2.9 ± 0.2	3.7 ± 0.2	3.8 ± 0.2	12×10^{-3}
$6 \times 10^{-10} \text{ A}$	2.9 ± 0.2	4.1 ± 0.1	4.2 ± 0.1	9×10^{-3}
$6 \times 10^{-9} \text{ A}$	3.4 ± 0.2	4.4 ± 0.3	4.5 ± 0.3	15×10^{-3}
$6 \times 10^{-8} \text{ A}$	3.4 ± 0.2	4.7 ± 0.3	4.9 ± 0.3	15×10^{-3}

Table 3. Measurement Results for $0.1\mu\text{m}$ active layer, Boone Heterostructure #9

2. Slope Analysis Limitations and the Low Injection Limit

As can be seen from the tabulated values, increasing probe current tends to increase the effective radius of the generation region, as expected and reported previously in ref [17]. The diffusion length as measured by both techniques is relatively constant as a function of probe current below $6 \times 10^{-8} \text{ A}$ in accordance with our model assumptions. Also evident is the disparity between the slope analysis method and the model fit. This difference is expected and is related to the degree to which the slope analysis limiting assumption of large Bessel function argument is valid. That is, the slope analysis predictions assume that we are in a regime where the Bessel function

argument $\frac{r}{L_d} \gg 1$. In this case, measurements were taken over a distance of 7-14 μm from the center point. Assuming an L_d actual of 4 μm we can estimate the degree of disparity that should result by consulting Figure 9. Entering the X-axis with a value of 7/4 or 2.5 we extract a Talmadge factor of 0.75, or we would expect that the slope analysis method would predict a value within 75% of the actual. This corresponds well to the ratio of the model fit prediction to slope analysis prediction 3 $\mu\text{m}/4\mu\text{m}$ - or 0.75. The lowest probe current shows the limits due to noise in this analysis. As expected, the slope analysis method will be impacted more greatly by poor signal to noise ratios because of its higher spatial resolution.

The figures that follow show the comparison between slope analysis plots and model fit plots. It is instructive to observe which portions of the model fits begin to deviate from the experimental data for higher probe currents. The trend away from low injection can be tracked by observing the deviation in the "shoulder" regions of the distributions as the probe current increases, (Figures 20,21, and 22.)

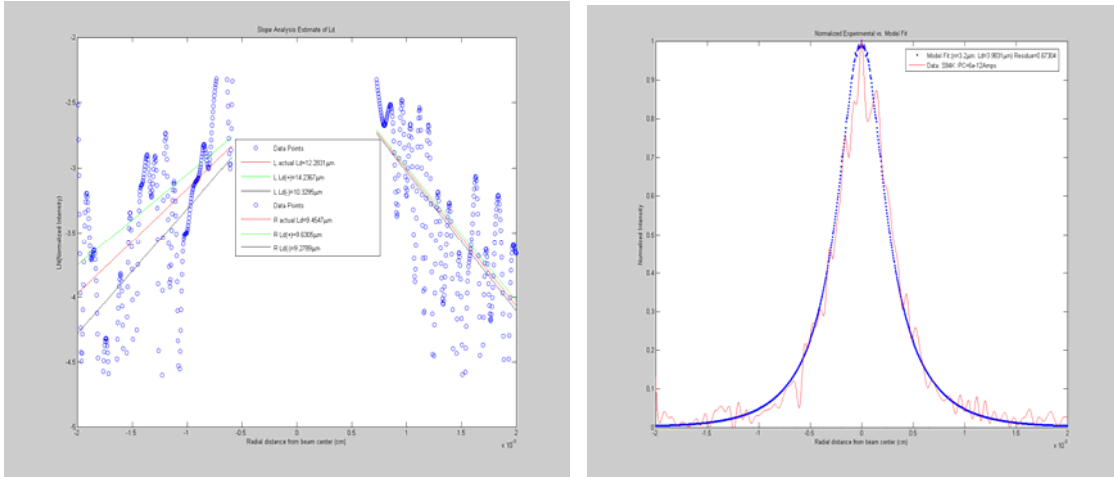


Figure 18. Slope and Model fit analysis plots for $6 \times 10^{-12} A$ probe current (pertinent data tabulated in Table 3)

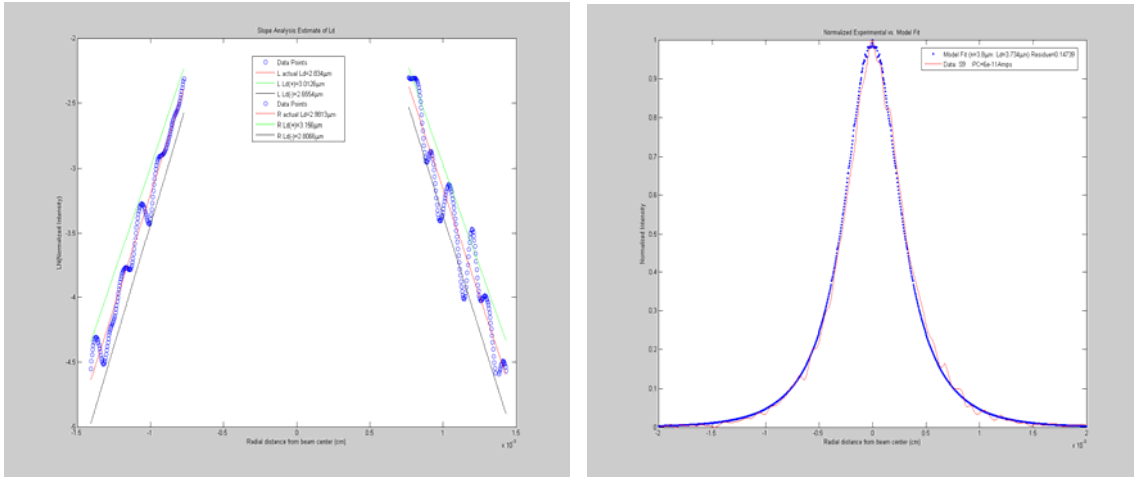


Figure 19. Slope and Model fit analysis plots for $6 \times 10^{-11} A$ probe current (pertinent data tabulated in Table 3)

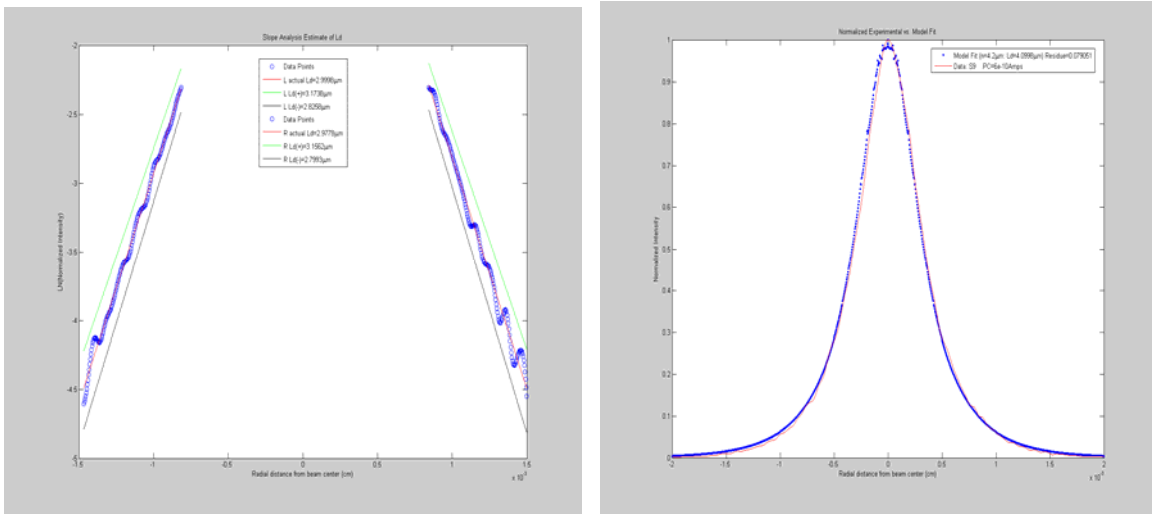


Figure 20. Slope and Model fit analysis plots for $6 \times 10^{-10} A$ probe current (pertinent data tabulated in Table 3)

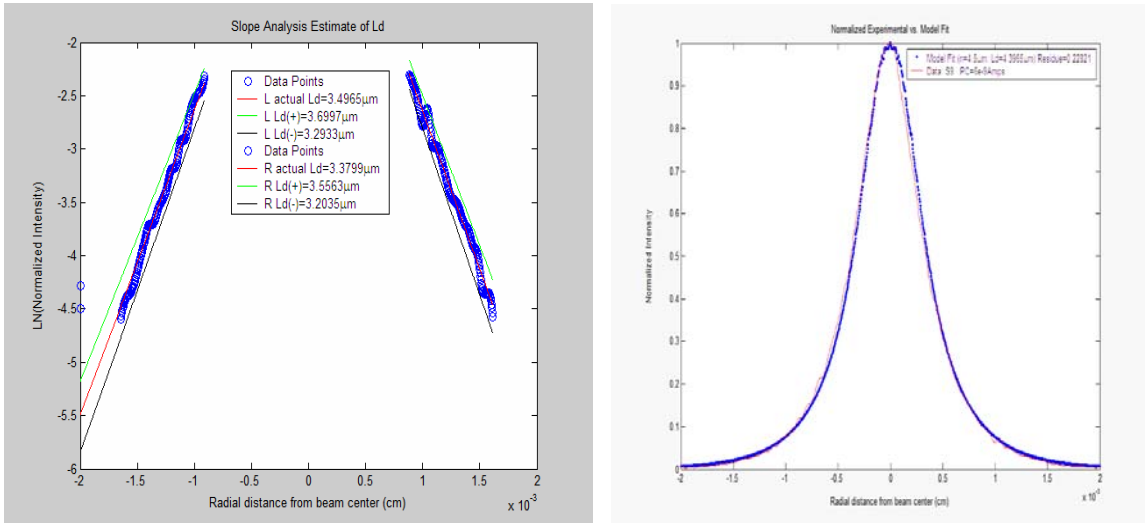


Figure 21. Slope and Model fit analysis plots for $6 \times 10^{-9} A$ probe current (pertinent data tabulated in Table 3)

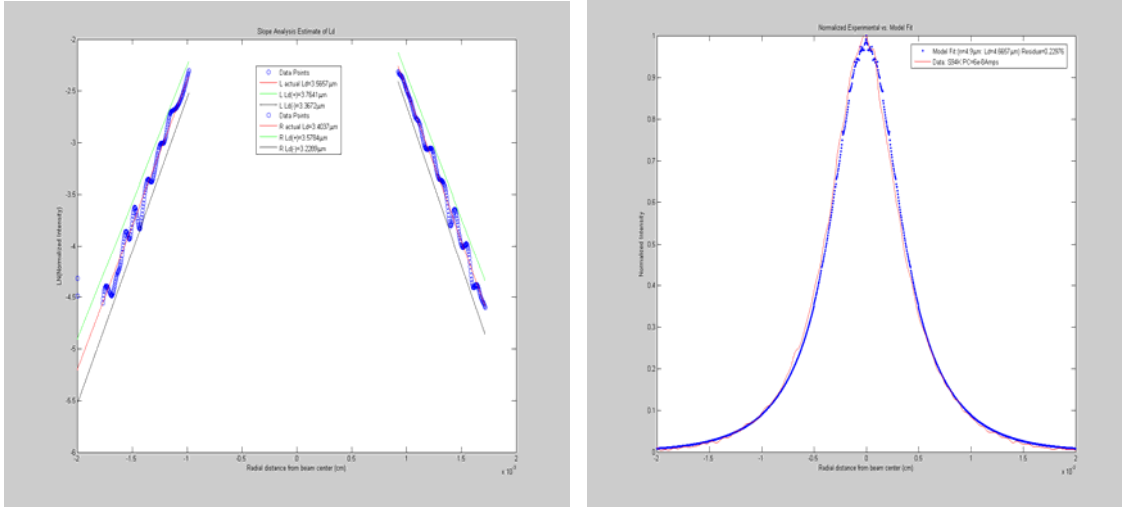


Figure 22. Slope and Model fit analysis plots for $6 \times 10^{-8} A$ probe current (pertinent data tabulated in Table 3)

From Table 3 we can see that the balance between signal to noise, and model limitations place the best probe current for accurate measurement at $6 \times 10^{-10} A$ for this sample.

3. Small Diffusion Length Limitations and the Role of the Generation Distribution

A more substantive measurement limitation for the heavily doped materials discussed in Chapter I is the relatively small diffusion lengths that accompany such large concentrations of acceptor dopants. While the literature predicts an increase in the minority electron mobility in GaAs doped with Be starting at $5 \times 10^{-18} cm^{-3}$, [23] the lifetime continues to trend downward at a rate which overpowers the increase in mobility and causes diffusion lengths to continue to decrease. Just beyond this concentration the diffusion length drops below $1 \mu m$, and we approach another limit of our technique. This limit is directly related to the generation region. In order to see

how this limit arises, we again study our solution to the transport equation for a Gaussian generation distribution.

$$(16) \quad n(x, y) = \frac{1}{2\pi L^2} \int_0^{2\sqrt{2}\sigma} K_o \left(\frac{\sqrt{S^2 + 4L^2}}{2L^2} |r - r'| \right) e^{\frac{S(x' - x)}{2L^2}} e^{\frac{-r'^2}{2\sigma^2}} dr'$$

Here the two terms which contribute to a zero E field ($S=0$) diffusion are the Bessel function and the Gaussian source function. As previously discussed, our use of the Bessel Equation comes from well-established differential equation theory for solving diffusion equations in 2D carrier transport and other disciplines governed by the Helmholtz Equation. The assumption of the Gaussian distribution to represent the carrier generation region within the sample is based upon the statistical interpretation of the electron-electron scattering and in limited cases is backed by empirical evidence [18],[20],[21].

More recently, work in our lab has shown that these distributions may not all fit the same mathematical dependence [19]. By assuming a standard Gaussian distribution, we may be neglecting effects of small deviations due to sample geometry, beam inhomogeneities, and possibly other effects that govern the sub-micrometer scale granularity of the minority carrier distribution. These inaccuracies in our model will become more prevalent when materials of small diffusion length are studied. Moreover, it is anticipated that when materials which have diffusion lengths on the order of our optical resolution are studied, it will become difficult to observe the effect of diffusion on the distribution. At this limit we may say

that we are indeed observing the generation region itself. As we approach this limit, the accuracy of our representation of the interaction region will become increasingly important. Any deviation of the actual distribution from our Gaussian model will be reflected in some mixture of parameter adjustments, which will unrealistically be portrayed as diffusion length or sigma variation by the fitting algorithm.

In order to make a quantitative assessment of this limit we will demonstrate a limiting case. By producing a distribution data set defined as a pure Gaussian ($n=3.0\mu\text{m}$) and allowing the fitting algorithm to fit Equation (16) to it, we may see what a material with no diffusion and a perfect Gaussian generation distribution might look like. Figure 23 shows the slope analysis and model fit for this case and demonstrates that both methods inaccurately predict a diffusion length of $0.3\mu\text{m}$. As predicted, the model fit compromises the generation region radius of the distribution from its known value of $3.0\mu\text{m}$ in order to fit the data with a diffusion length that allows for the smallest residue permissible.

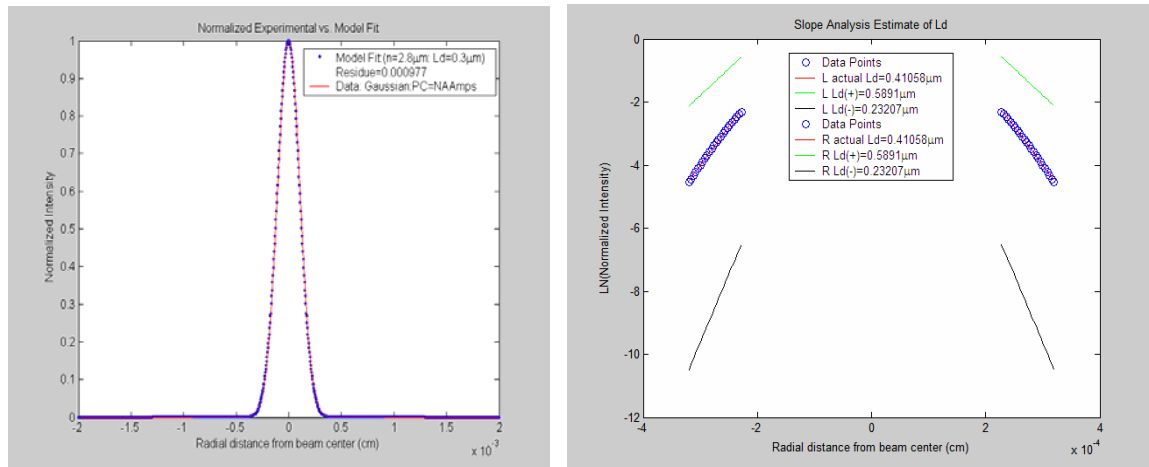


Figure 23. Pure Gaussian Distribution Model Fit

In other limiting cases where the modeled data set was produced with very small but non-zero diffusion lengths, the algorithm's accuracy was directly proportional to the step size, (analogous to pixel size) used in the creation of the data. This is consistent with our prediction that our CCD pixel size results in an effective lower limit of discernability $0.4\mu\text{m}$ for either parameter value. However, because the generation distribution radius does not approach this lower value, it is effectively only a limit for our determination of diffusion lengths. Compounding this lower limit is any inaccuracy in our assumption of generation region form, which will tend to distort both σ and L_d . As we approach the regime where the form of the generation distribution contributes more than does diffusion to the shape of the overall distribution we expect this limitation to have a larger and larger effect. Moreover, the $0.4\mu\text{m}$ error suggested above is only accurate when you assume a perfect Gaussian generation region. Any deviation of the generation region from the ideal will tend to increase our baseline error.

In reference [19] Luber discusses the use of this same Transport Imaging technique as a means to more accurately determine the interaction region distribution for materials of interest. While a full quantitative method has not been developed, it is seen as a key step toward the study of very small diffusion length materials ($L_d \leq 1.0\mu\text{m}$).

V. STUDY OF HEAVILY DOPED HETEROSTRUCTURES

A. MOTIVATION

As discussed in Chapter I, faster switching transistors are of prime importance to military applications. The devices that are currently under development to handle this task, in commercial applications as well as military, are HBTs. The key device parameter for increasing speed and efficiency is the base layer transit time. Many engineering design approaches are used to decrease the time it takes electrons to flow across the base layer, but the efficient use of these techniques is dependent upon the accurate knowledge of the transport properties - minority electron diffusion length, lifetime, and mobility.

A mathematical description of the base transit time reveals the importance of low dimension construction as well.

$$(18) \quad \tau_B = \frac{W^2}{2D_p}$$

where τ_B is the base transit time, W is the base width, and,

$$(19) \quad D_p = \frac{\mu_p kT}{e}$$

is the minority carrier diffusion coefficient as defined by the Einstein equation where μ_p is the minority carrier mobility, e the charge on an electron, k Boltzmann's constant, and T is the temperature in Kelvins [1].

The appearance of the base width as a squared term dominates the trend of transit time, but with decreased

base width comes the problem of emitter-collector current leakage. Here, increased dopant concentrations aid the reduction of the base width by providing an impediment to this current leakage, however, classical analysis predicts that increased doping has a negative effect on τ_B through its reduction of μ_p and therefore D_p [1]. Classically, one would predict a practical limit to the concentration of dopants that can be used as the competing effects of reduced D_p and decreased W interact. However, a more detailed analysis reveals a more complex picture.

B. QUANTUM MECHANICAL PREDICTIONS

An observation of nonconventional electron current density in an GaAs/AlGaAs N-p-n HBT with Be base doping of $6 \times 10^{18} cm^{-3}$ led Lyon and Casey to believe that some other transport mechanism was at play. They observed a collector-emitter current density that exceeded conventional predictions by four times [29]. More recently, material growth techniques have improved and base layers are being produced with graded doping schemes in the low $10^{20} cm^{-3}$ [5]. At these levels the assumptions of the Boltzmann distribution and classical carrier scattering descriptions may not be sufficient to explain carrier transport. In work done by Bennett and Lowney employing a first principles quantum mechanical analysis of scattering mechanisms in heavily doped GaAs, it is predicted that a local minima exists for electron mobility in the $5 \times 10^{18} cm^{-3}$ regime. This analysis includes all the important scattering mechanisms for the low-field mobilities: acoustic phonon, polar optic phonon, piezoelectric, ionized

impurity, carrier-carrier, alloy, and plasmon scattering. The upturn in the mobility results from the dependence of these scattering mechanisms on the dopant and carrier density. As the dopant density increases the average distance between holes decreases. This screening radius then determines the upper frequency that may be supported for the vibrational modes set up in the plasma of majority carrier holes, plasmon cutoff frequency (PCF). As the PCF increases, the scattering interaction probability between minority carrier electrons and plasmons decreases. Additionally, as the free hole concentration increases the lower energy bands fill, and Pauli Exclusion Principle screening becomes important. The number of majority carrier/minority carrier scattering events is reduced because the holes are precluded from changing their energy level and therefore can not interact [23].

These results have been difficult to reinforce experimentally and limited direct evidence exists to support them [25-28]. A method to observe this effect in a non-contact manner which requires little sample preparation and is non-invasive would add to existing device diagnostics techniques. Transport Imaging provides such a solution.

C. EXPERIMENTAL RESULTS

In order to observe this increasing mobility trend a series of Be doped heterostructures was studied. Figure 24 shows the design of the studied structures.

$\text{Ga}_{0.6}\text{Al}_{0.4}\text{As}$: $0.2\mu\text{m}$; p- $5 \times 10^{18} \text{ cm}^{-3}$	electron confinement
Grading: 500 Å	interface recombination
$\text{Ga}_{0.6}\text{Al}_{0.4}\text{As}$: $1.0\mu\text{m}$; $N_A - 3 \times 10^{18} - 1 \times 10^{20} \text{ cm}^{-3}$	PL active region peak emission $\approx 870\text{nm}$
Grading: 500 Å	interface recombination
$\text{Ga}_{0.6}\text{Al}_{0.4}\text{As}$: $0.2\mu\text{m}$; p- $5 \times 10^{18} \text{ cm}^{-3}$	electron confinement

Figure 24. Heterostructure design as grown by Tom Boone,
(From Ref. [22])

The Transport Imaging technique was applied to seven samples of differing active layer doping and the diffusion length of the samples was extracted using both the slope analysis method and the two parameter fit. Data were taken at multiple locations on each sample, on different days and under varying beam energy and probe currents. Though some variation of parameter value with location was noted, overall the samples can be considered to be very homogeneous, and these results to be representative of the average properties. In order to test the predictions of Dr. Bennett, we required lifetime (τ) values with which we could extract mobility (μ) values from our diffusion length measurements through the relationship of Equations (3) and (18). We coupled independent measurements of the sample lifetimes with values provided by the grower, Dr. Boone. In both cases the measurements were made by time resolved photo-luminescence techniques. Table 4 tabulates the

initial measured values for these samples. The lifetimes marked with an asterisk were measured in 2003-2004 by Yale University and were not corroborated by our independent and more accurate TRPL confirmation. Comparisons between the Yale reported lifetimes and our TRPL measurements for the other samples showed a 10% overestimation in the samples of with $\text{Na} > \times 10^{19} \text{ cm}^{-3}$.

Sample	Doping [cm^{-3}]	τ [ps]	L_d [μm]	μ $\left[\frac{\text{cm}^2}{\text{V} \cdot \text{s}} \right]$
A2	2.75×10^{18}	$2050 *$	$3.6 \pm .1$	2500 ± 140
B7	3.75×10^{18}	900	$2.3 \pm .1$	2350 ± 200
C9	$5 \times 10^{18} \pm 3 \times 10^{18}$	4800	$4.1 \pm .1$	1333 ± 68
D6	3.5×10^{19}	95	$1.6 \pm .2$	10800 ± 2800
E3	4.0×10^{19}	$140 *$	$1.8 \pm .15$	9200 ± 1600
F4	6×10^{19}	$116 *$	$1.9 \pm .1$	12400 ± 1300
G8	$1.0 \times 10^{20} \pm .1 \times 10^{20}$	11	$1.7 \pm .2$	101000 ± 25300

Table 4. Initial results of AlGaAs/GaAs heterostructure study

1. Initial Observations

The result for sample C9 is the only sample that is completely consistent with Dr. Bennett's predictions. It is also the sample tested in Chapter III, and possesses an active layer dimension 10 times thinner than the other samples. Samples B2 and C7 are consistent with Bennett's trend of decreasing mobility toward the inflection point at a concentration of $5.0 \times 10^{18} \text{ cm}^{-3}$ though offset by approximately $1000 \frac{\text{cm}^2}{\text{V} \cdot \text{s}}$. Other reported data for mobilities in this range

of doping concentrations also show elevated values compared with Bennett's predictions [24]. However, the mobilities for samples D-G are unrealistic, even if the trend of increasing mobility is evident.

The consistent positive offset of these values suggests a systemic error or effect that is operational in the $>10^{19}\text{cm}^{-3}$ samples. We propose two reasons for these offsets and apply appropriate offsets to account for them.

2. Generation Region Discrepancies

As mentioned in paragraph B, we expect that as we approach the regime where the generation region contributes more and more to the shape of the extracted curve, we will be subject to limitations due to inaccurate assumptions about the generation region. By studying the curve fits in the higher doped samples we can gain some intuition about where this limit may be. The figures that follow (Fig. 25-28) are the best residue curve fit achieved for each of the samples.

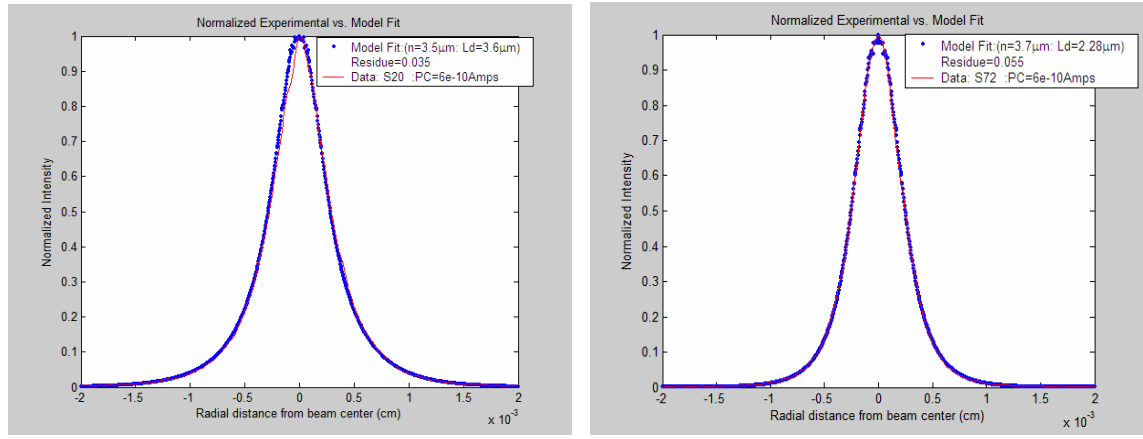


Figure 25. Samples A2 and B7 best fit 2-parameter fit extractions

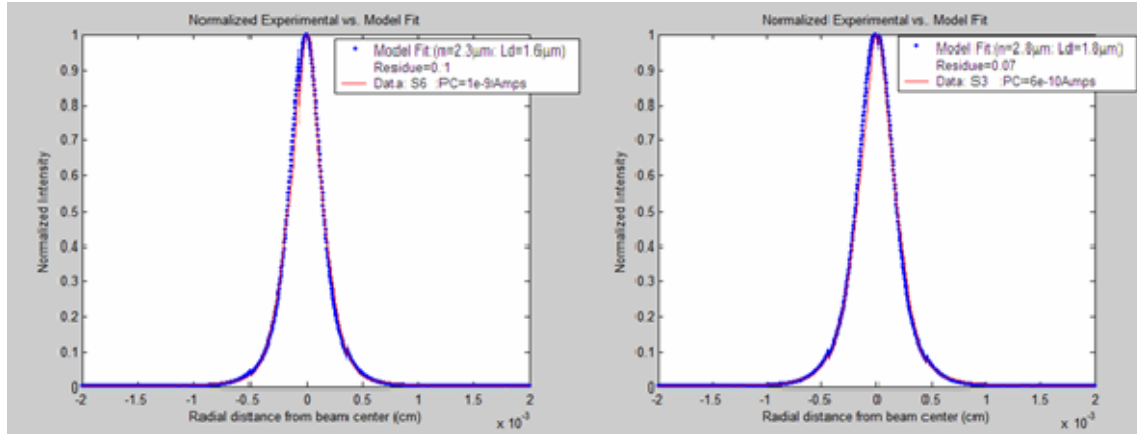


Figure 26. Samples D6 and E3 best fit 2-parameter fit extractions

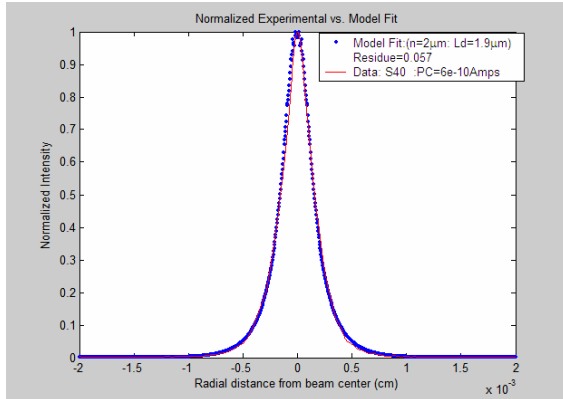


Figure 27. Sample F4 best fit 2-parameter fit extraction

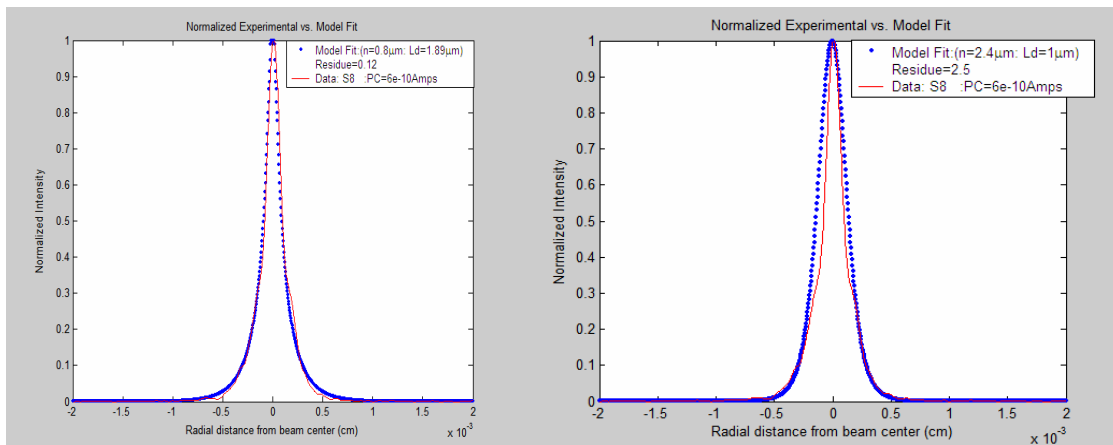


Figure 28. Sample G8 best fit (a) algorithm run, (b) Assumed reasonable generation region with algorithm fitted diffusion length

The generation region radius has been shown to increase with probe current and with beam energy, but here we see a decrease in the generation region as a function of dopant concentration. Also noted is the tendency of the model fit to depart from the data set in the region of the shoulders of the curves near the base of the distribution. This effectively causes an overestimation of the diffusion lengths as predicted in Section B. Finally, we can surmise that in samples D-G we are in the realm where the diffusion lengths are on the order of the generation region radius, or less, and approaching a fundamental limit of our assumptions. If we assume that the produced error is on the order of that demonstrated with the pure Gaussian from Chapter IV, Section C. we would expect an overestimation of the diffusion length by $0.4\mu\text{m}$.

3. Photon Recycling (PR)

Another important and well-documented effect that must be considered is that of Photon Recycling. The literature is replete with documentation of this phenomenon that affects diffusion coefficients and observed lifetimes in bulk GaAs that begins to act in this doping regime [30-32]. The effect is treated in different manners, but consistently results in correction terms being used to adjust the observed diffusion coefficient and total lifetime. Renaud treats the effect as an addition to the generation function in the continuity equation (our Equation (10)). He defines the photon recycling generation function: [30]

$$(20) \quad G_{PR} = \frac{\alpha_i}{2\tau_r} \int_0^w K(x, x') \Delta n(x', t) dx'$$

This represents the excitation in the sample with thickness w and average absorption coefficient α , taking into account the spectral density of the light. τ_r is the radiative lifetime related to the lifetime we measure with TRPL by

$$(21) \quad \frac{1}{\tau} = \frac{1}{\tau_r} + \frac{1}{\tau_{nr}}$$

where τ_{nr} is the non-radiative lifetime. The real perturbation comes from the calculation of $K(x,x')$, which is related as a series of exponential integral functions [30]. The minority carrier distribution is then expanded in a series expansion over the photon recycling source region and the continuity equation is now adjusted with each term possessing a PR perturbation factor T_n , where:

$$(22) \quad T_n = \frac{1}{n!} \frac{\alpha_i}{\tau_r} \int_{-x}^{w-x} K(x, x+u) u^n du$$

Because K is principally a function of exponential integral functions and converges quickly to zero with increasing n , they can be represented by the spatial average value $\langle T_n \rangle$. Appendix B lists the first two non-zero terms of this series: $\langle T_0 \rangle$ and $\langle T_2 \rangle$ in their full mathematical form, as well as the exponential integral function. The resulting continuity equation is a modification of our Equation (4.5):

$$(23) \quad 0 = G_n - \left(\frac{1}{\tau_n} - \langle T_0 \rangle \right) n - \mu_n E \frac{dn}{dx} + \left(\frac{L^2}{\tau_n} + \langle T_2 \rangle \right) \vec{\nabla}^2 n$$

Renaud demonstrates good agreement between his corrective terms and behavior of GaAs LEDs and photovoltaic

cells, and calls for more study on small thickness samples. Badescu states that while photon recycling is most apparent in bulk samples, there is a more pronounced effect in samples where the absorption length $L_\alpha \equiv \frac{1}{\alpha}$ exceeds the diffusion length, even for thinner samples ($< 1\mu\text{m}$) [31].

If we add a column to Table 4 and populate it with the absorption coefficient α (taken from [33]) and the absorption length for each sample we see a correlation between the departure from predicted values of mobility and the breakpoint where absorption length exceeds diffusion length.

Sample	Doping [cm^{-3}]	τ [ps]	L_d [μm]	α [μm^{-1}]	L_α [μm]	μ [$\frac{\text{cm}^2}{\text{V}\cdot\text{s}}$]
A2	2.75×10^{18}	$2050 *$	$3.6 \pm .1$	5000	2.0	2500 ± 140
B7	3.75×10^{18}	900	$2.3 \pm .1$	4500	2.2	2350 ± 200
C9	$5 \times 10^{18} \pm 3 \times 10^{18}$	4800	$4.1 \pm .1$	4000	2.5	1333 ± 68
D6	3.5×10^{19}	95	$1.6 \pm .2$	3500	2.85	10800 ± 2800
E3	4.0×10^{19}	$140 *$	$1.8 \pm .15$	3400	2.94	9200 ± 1600
F4	6×10^{19}	$116 *$	$1.9 \pm .1$	3000	3.3	12400 ± 1300
G8	$1.0 \times 10^{20} \pm .1 \times 10^{20}$	11	$1.7 \pm .2$	2300	4.3	101000 ± 25300

Table 5. HS data table with absorption length comparison

C. CORRECTIONS FOR OPERATIVE EFFECTS AND DISCUSSED LIMITATIONS

The photon recycling effect is dependent upon the number of photons generated, the rate at which they reabsorb, but also on the rate at which they can escape the active layer before creating additional electron-hole pairs. The first dependencies we have previously described, but now we must look at the index of refraction of our samples and the corresponding critical angle of total internal reflection.

In 1976 Asbeck reported the critical angle for GaAs/AlGaAs interfaces as a function of various Al concentrations [35]. Interpolating from his graphs and confirming with Snell's Law, we arrive at a critical angle for the active GaAs layer of 69.6° . The index of refraction varies with dopant density as well, but because the differences are small between AlGaAs and GaAs we can use the value for GaAs as 3.59 and for 40% Al concentration in AlGaAs $n=3.36$. Using these values to calculate the Reflectance; [36]

$$(23) \quad R = \left(\frac{1-n}{1+n} \right)^2$$

For $n = \frac{n_{AlGaAs}}{n_{GaAs}} = \frac{3.36}{3.59} = .935$ and therefore $R = 0.1\%$, or when light strikes the interface at an angle less than the critical angle, 99.9% will transmit through to the AlGaAs layer. Also required is the radiative lifetime. From [32] we can define:

$$(24) \quad \tau_r = \frac{1}{2 \times 10^{-10} \cdot N_A} [s]$$

Now to calculate the correction factors and apply them to our experimental results for the samples in Tables 3 and 4 we employ the MATHCAD routine of Appendix B.1. The detailed calculation sheets are in Appendix B.x and the overall results are tabulated below in Table 6.

Sample	Doping [cm ⁻³]	τ [ps]	L_d^{**} [μm]	$\mu \left[\frac{cm^2}{V \cdot s} \right]$	τ_{PR} [ps]	L_{dPR} [μm]	$\mu_{PR} \left[\frac{cm^2}{V \cdot s} \right]$
A2	2.75×10^{18}	2050 *	$3.6 \pm .1$	2500 ± 140	NC	NC	NC
B7	3.75×10^{18}	900	$2.3 \pm .1$	2350 ± 200	NC	NC	NC
C9	$5 \times 10^{18} \pm 3 \times 10^{18}$	4800	$4.1 \pm .1$	1333 ± 68	NC	NC	NC
D6	3.5×10^{19}	95	$1.2 \pm .2$	6000 ± 2000	69	$1.0 \pm .2$	6000 ± 2000
E3	4.0×10^{19}	140 *	$1.4 \pm .15$	5600 ± 1300	85 *	$1.1 \pm .15$	5500 ± 1600
F4	6×10^{19}	116 *	$1.5 \pm .1$	7800 ± 1000	66 *	$1.0 \pm .1$	7600 ± 1300
G8	$1.0 \times 10^{20} \pm .1 \times 10^{20}$	11	$1.0 \pm .2$	59000 ± 20000	9	$0.9 \pm .2$	36000 ± 15300

Table 6. Tabulated Parameters corrected for Generation Region error(**) and Photon Recycling overestimation

D. CONCLUSIONS

The effect of the Generation Region (GR) error plays a much stronger role on the calculated mobility values than does Photon Recycling (PR) because of the simultaneous effect PR has on diffusion length and lifetime. The PR effect is seen to grow as a function of doping.

The assumption of a 0.4μm error for GR is an estimate that needs more refinement, through the development of an analytical assessment of generation region definition and its inclusion in the numerical integration algorithm of

Appendix A. Transport Imaging provides an appropriate mechanism for this analysis and should be pursued.

The mobility values from the final corrected column are plotted against Dr. Bennett's predicted results with appropriate error bars in Figure 29.

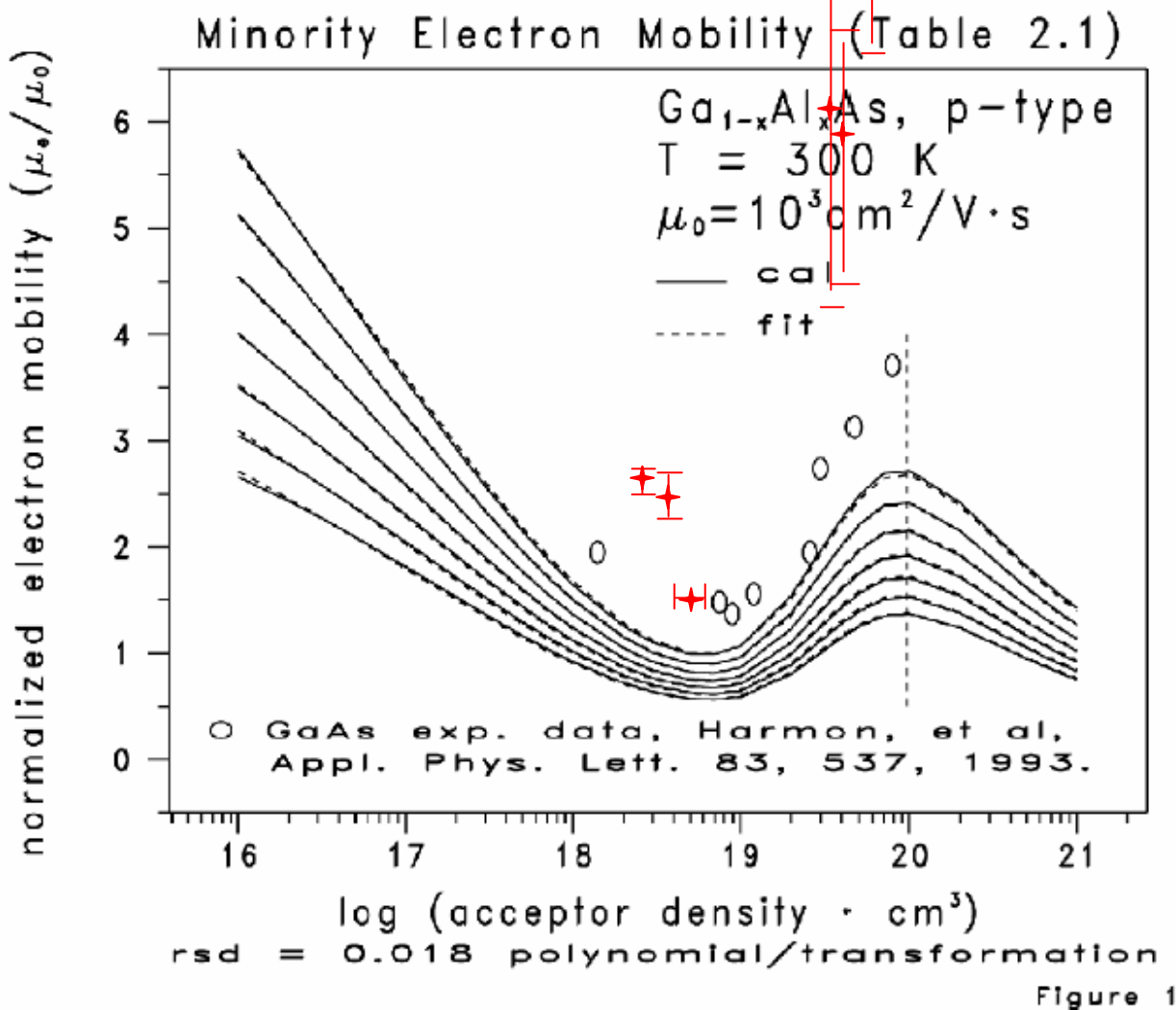


Figure 29. Final corrected Transport Imaging mobility values reported (After Bennett [9])

The local minimum is clearly demonstrated though absolute magnitude agreement is not. A new round of experiments is planned to test the magnitude relationships

of the $\mu\tau$ product through the measurement of L_{drift} by studying the distributions as a result of an applied DC bias. In this manner a full distribution fit should escape the limitations resulting from generation region error, though the optical resolution limitation ($0.4 \mu m$) may still be operative in the samples of heaviest concentrations.

From the results demonstrated it can be assumed that of the limitations and constraints inherent in Transport Imaging the assumption of a generation region distribution has the largest impact for measurement of low diffusion length materials. It appears that experimental results can be assumed valid so long as the diffusion length measured is on the order of the generation region radius (as in Samples A9-C2), that the signal to noise ratio is favorable (as in all data samples shown herein), and that the diffusion lengths measured are greater than the optical resolution of the system ($0.4\mu m$ in these data samples).

Several methods may be useful to overcome these constraints and are being studied in our laboratory. They include time resolved techniques reminiscent of the Haynes Shockley experiment, but maintaining the spatial information of the light emission to great resolution, AC drift techniques attempting to generate resonance responses between transport properties and the applied electric force, and observation of the effects of magnetic fields on the flow of the charge carriers at the sub micrometer scale.

APPENDIX A. TRANSPORT IMAGING GRAPHIC USER INTERFACE CODE

C:\Documents and Settings\FMBradley\My Document...\\newfirsttry.m Page 1
November 16, 2005 2:18:47 PM

```
1 function varargout = newfirsttry(varargin)
2
3 %-----Log of program changes-----
4 %29 August - changed mkdir location for gui directory creation to create
5 %within diffusive data analysis\analyzed data.
6 %Will change parameter matching to Ld versus Mobility
7 %19 September - updated version on laptop with amended version from desktop
8 %12 October - Cleaned up comments and reorganized order of functions
9 %16 October - Reset all flag values in each main analysis functions (aflag,gflag, fit
10 % flag) all tested for empty variable status and set to '0' if so.
11 % NEWFIRSTTRY Application M-file for newfirsttry.fig
12 %   NEWFIRSTTRY, by itself, creates a new NEWFIRSTTRY or raises the existing
13 %   singleton*.
14 %
15 % H = NEWFIRSTTRY returns the handle to a new NEWFIRSTTRY or the handle to
16 % the existing singleton*.
17 %
18 % NEWFIRSTTRY('CALLBACK', hObject, eventData, handles,...) calls the local
19 % function named CALLBACK in NEWFIRSTTRY.M with the given input arguments.
20 %
21 % NEWFIRSTTRY('Property','Value',...) creates a new NEWFIRSTTRY or raises the
22 % existing singleton*. Starting from the left, property value pairs are
23 % applied to the GUI before newfirsttry_OpeningFunction gets called. An
24 % unrecognized property name or invalid value makes property application
25 % stop. All inputs are passed to newfirsttry_OpeningFcn via varargin.
26 %
27 % *See GUI Options - GUI allows only one instance to run (singleton).
28 %
29 % See also: GUIDE, GUIDATA, GUIHANDLES
30
31 % Edit the above text to modify the response to help newfirsttry
32
33 % Last Modified by GUIDE v2.5 30-Mar-2005 12:09:12
34
35 % Begin initialization code - DO NOT EDIT
36
37 gui_Singleton = 1;
38 gui_State = struct('gui_Name',           mfilename, ...
39                   'gui_Singleton',        gui_Singleton, ...
40                   'gui_OpeningFcn',       @newfirsttry_OpeningFcn, ...
41                   'gui_OutputFcn',        @newfirsttry_OutputFcn, ...
42                   'gui_LayoutFcn',         [], ...
43                   'gui_Callback',          []);
44 if nargin & isstr(varargin{1})
45     gui_State.gui_Callback = str2func(varargin{1});
46 end
47
48 if nargout
```

```
49     varargout{1:nargout} = gui_mainfcn(gui_State, varargin{:});
50 else
51     gui_mainfcn(gui_State, varargin{:});
52 end
53 % End initialization code - DO NOT EDIT
54 %Initialize global variables
55 global aflag gflag foldername firsttime fitflag;
56 %aflag=0;
57 %gflag=0;
58 %fitflag=0;
59 %firsttime=0;
60 filetoload=[];
61
62 %
63 % --- Executes just before newfirsttry is made visible.
64 function newfirsttry_OpeningFcn(hObject, eventdata, handles, varargin)
65 % This function has no output args, see OutputFcn.
66 % hObject    handle to figure
67 % eventdata   reserved - to be defined in a future version of MATLAB
68 % handles    structure with handles and user data (see GUIDATA)
69 % varargin   command line arguments to newfirsttry (see VARARGIN)
70
71 % Choose default command line output for newfirsttry
72 handles.output = hObject;
73
74 % Update handles structure
75 guidata(hObject, handles);
76
77 if nargin == 3,
78     initial_dir = pwd;
79 elseif nargin > 4
80     if strcmpi(varargin{1}, 'dir')
81         if exist(varargin{2}, 'dir')
82             initial_dir = varargin{2};
83         else
84             errordlg('Input argument must be a valid directory', 'Input Argument Error!');
85         return
86     end
87 else
88     errordlg('Unrecognized input argument', 'Input Argument Error!');
89     return;
90 end
91 end
92 % Populate the listbox
93 load_listbox(initial_dir, handles)
94 % Return figure handle as first output argument
95
```

```
96 % UIWAIT makes newfirsttry wait for user response (see UIRESUME)
97 % uiwait(handles.newfirsttry);
98
99 %


---


100 % --- Outputs from this function are returned to the command line.
101 function varargout = newfirsttry_OutputFcn(hObject, eventdata, handles)
102 % varargout cell array for returning output args (see VARARGOUT);
103 % hObject handle to figure
104 % eventdata reserved - to be defined in a future version of MATLAB
105 % handles structure with handles and user data (see GUIDATA)
106
107 % Get default command line output from handles structure
108 varargout{1} = handles.output;
109
110 %


---


111 % Callback for list box - open .fig with guide, otherwise use open
112 % -----
113 function varargout = listbox1_Callback(hObject, eventdata, handles)
114 % hObject handle to listbox1 (see GCBO)
115 % eventdata reserved - to be defined in a future version of MATLAB
116 % handles structure with handles and user data (see GUIDATA)
117
118 % Hints: contents = get(hObject,'String') returns listbox1 contents as cell array
119 %         contents{get(hObject,'Value')} returns selected item from listbox1
120
121 get(handles.newfirsttry,'SelectionType');
122 global filetoload tiftoload ;
123
124 if strcmp(get(handles.newfirsttry,'SelectionType'),'open')
125     index_selected = get(handles.listbox1,'Value');
126     file_list = get(handles.listbox1,'String');
127     filename = file_list(index_selected);
128     if handles.is_dir(handles.sorted_index(index_selected))
129         cd (filename)
130         load_listbox(pwd,handles)
131     else
132         [path,name,ext,ver] = fileparts(filename);
133         switch ext
134             case '.fig'
135                 guide (filename)
136             case '.tif'
137                 tiftoload=filename;
138             case '.csv'
139                 filetoload=filename;
140             otherwise
141                 try
142                     filetoload=filename;
```

```
143     catch
144         errordlg(lasterr,'File Type Error','modal')
145     end
146     end
147 end
148 end
149 % _____  
  
150 % Read the current directory and sort the names
151 % -----
152 function load_listbox(dir_path,handles)
153 cd (dir_path)
154 dir_struct = dir(dir_path);
155 [sorted_names,sorted_index] = sortrows({dir_struct.name});
156 handles.file_names = sorted_names;
157 handles.is_dir = [dir_struct.isdir];
158 handles.sorted_index = [sorted_index];
159 guidata(handles.newfirsttry,handles)
160 set(handles.listbox1,'String',handles.file_names, ...
161      'Value',1)
162 set(handles.text1,'String',pwd)
163 %
164 % _____  
  
165 % --- Executes during object creation, after setting all properties.
166 function listbox1_CreateFcn(hObject, eventdata, handles)
167 % hObject    handle to listbox1 (see GCBO)
168 % eventdata reserved - to be defined in a future version of MATLAB
169 % handles    empty - handles not created until after all CreateFcns called
170
171 % Hint: listbox controls usually have a white background, change
172 %       'usewhitebg' to 0 to use default. See ISPC and COMPUTER.
173 usewhitebg = 1;
174 if usewhitebg
175     set(hObject,'BackgroundColor','white');
176 else
177     set(hObject,'BackgroundColor',get(0,'defaultUicontrolBackgroundColor'));
178 end
179 %
180 % _____  
  
181 % --- Executes during object creation, after setting all properties.
182 function edit2_CreateFcn(hObject, eventdata, handles)
183 % hObject    handle to edit2 (see GCBO)
184 % eventdata reserved - to be defined in a future version of MATLAB
185 % handles    empty - handles not created until after all CreateFcns called
186
187 % Hint: edit controls usually have a white background on Windows.
188 %       See ISPC and COMPUTER.
```

```
189 if ispc
190     set(hObject,'BackgroundColor','white');
191 else
192     set(hObject,'BackgroundColor',get(0,'defaultUicontrolBackgroundColor'));
193 end
194
195 %
196 % --- Executes on mouse press over axes background.
197 function newname_ButtonDownFcn(hObject, eventdata, handles)
198 % hObject    handle to newname (see GCBO)
199 % eventdata   reserved - to be defined in a future version of MATLAB
200 % handles    structure with handles and user data (see GUIDATA)
201
202 %
203 % --- Executes on button press in pushbutton1. (Vector Data Manipulator = vdatamanipulator)
204 function pushbutton1_Callback(hObject, eventdata, handles)
205 % hObject    handle to pushbutton1 (see GCBO)
206 % eventdata   reserved - to be defined in a future version of MATLAB
207 % handles    structure with handles and user data (see GUIDATA)
208 global filetoload aflag gflag foldername fitflag;
209 if (aflag==[]) aflag=0;
210 end
211 if (gflag==[]) gflag=0;
212 end
213 if (fitflag==[]) fitflag=0;
214 end
215 %Determine if this is a current session or a return to a previous session of data creation
216 button = questdlg('Are you in an active session of data analysis?','Session Type Selection');
217 switch button
218 case 'Yes'
219     nott='not';
220     [Valmanac,xnplot,ynplot,xinterp,yinterp,sample_name,BeamEnergy,probe_current] =vdatamanipulator(filetoload, aflag, gflag, foldername);
221     almanac_save(Valmanac,foldername,xnplot,ynplot,xinterp,yinterp,gflag,nott,filetoload);
222     if fitflag
223         datatofit=[xinterp;yinterp];
224         fbsLd(datatofit,foldername,sample_name,BeamEnergy,probe_current);
225     end
226 case 'No'
227     prompt = {'Enter the folder name for data plot storage','Enter name of superposition plot to amend'};
228     dlg_title = 'Amended Session Input';
229     num_lines= 1;
```

```
230     def      = {'',''};  
231     answer  = inputdlg(prompt,dlg_title,num_lines,def);  
232     answerstr=char(answer);  
233     of=answer(1);  
234     oldfolder=char(of)  
235     superplotname=char(answerstr(2,:));  
236     [Valmanac,xnplot,ynplot,xinterp,yinterp,sample_name,BeamEnergy,probe_current] =  
=ydatamanipulator(filetoload, aflag1, gflag1, oldfolder);  
237     almanac_save(Valmanac,oldfolder,xnplot,ynplot,xinterp,yinterp,gflag,superplot,  
name,filetoload);  
238     if fitflag  
239         datatofit=[xinterp;yinterp]';  
240         fbsLd(datatofit,foldername,sample_name,BeamEnergy,probe_current);  
241     end  
242 otherwise  
243     disp('To find the superplot and folder to amend, look in SEM\\. Folder data se  
ts are named by a 1xLetter designator denoting sample, followed by the beam energy.   
The superplot is in this folder.')  
244 end  
245  
246 %  
  
247 % --- Executes on button press in pushbutton2 (ImageDataManipulator)  
248 function pushbutton2_Callback(hObject, eventdata, handles)  
249 % hObject handle to pushbutton2 (see GCBO)  
250 % eventdata reserved - to be defined in a future version of MATLAB  
251 % handles structure with handles and user data (see GUIDATA)  
252 global tiftoload foldername aflag gflag fitflag;  
253 if (aflag==[]) aflag=0;  
254 end  
255 if (gflag==[]) gflag=0;  
256 end  
257 if (fitflag==[]) fitflag=0;  
258 end  
259 %Determine if this is a current session or a retur  
rn to a previous session of data creation  
260 button = questdlg('Are you in an active session of data analysis?','Session Type Sele  
ction','Cancel');  
261 switch button  
262 case 'Yes'  
263     nott='not';  
264     [almanacR, almanacC,xnplot,ynplot,xinterp,yinterp,sample_name,BeamEnergy,prob  
e_current]=imagedatamanipulator(tiftoload, aflag, gflag, fitflag, foldername);  
265     almanac_save(almanacR,foldername,xnplot,ynplot,xinterp,yinterp,gflag,nott,tif  
toload);  
266     flagc=0; %Sets the superimposition flag to '0' so column data   
will not be printed on superposition plot  
267     almanac_save(almanacC,foldername,xnplot,ynplot,xinterp,yinterp,flagc,nott,tif  
toload);
```

```
268     if fitflag
269         datatofit=[xinterp;yinterp]';
270         fbsLd(datatofit,foldername,sample_name,BeamEnergy,probe_current);
271     end
272 case 'No'
273     prompt = {'Enter the folder name for data plot storage','Enter name of superposition plot to amend'};
274     dlg_title = 'Amended Session Input';
275     num_lines= 1;
276     def      = {'',''};
277     answer  = inputdlg(prompt,dlg_title,num_lines,def);
278     answerstr=char(answer);
279     oldfolder=(answerstr(1,:));
280     superplotname=(answerstr(2,:));
281     nott='not';           %Ensures that column data will not be
282     [almanacR, almanacC,xnplot,ynplot,xinterp,yinterp,sample_name,BeamEnergy,prob
e_current]=imagedatamanipulator(tiftoload, aflag, gflag, fitflag, oldfolder);
283     almanac_save(almanacR,foldername,xnplot,ynplot,xinterp,yinterp,gflag,superplot
tname,tiftoload);
284     flagc=0;             %Sets the superimposition flag to '0' so column data will
not be printed on superposition plot
285     almanac_save(almanacC,foldername,xnplot,ynplot,xinterp,yinterp,flagc,nott,tif
toload);
286     if fitflag
287         datatofit=[xinterp;yinterp]';
288         fbsLd(datatofit,foldername,sample_name,BeamEnergy,probe_current);
289     end
290 otherwise
291 disp('To find the superplot and folder to amend, look in SEM\\. Folder data sets ar
e named by a 1xLetter designator denoting sample, followed by the beam energy. The su
perplot is in this folder.')
292
293 end
294
295 %
296 % --- Executes on upcheck of checkbox1 = This is for 'Keep Almanac for mulitple files'.
297 function checkbox1_Callback(hObject, eventdata, handles)
298 % hObject    handle to checkbox1 (see GCBO)
299 % eventdata   reserved - to be defined in a future version of MATLAB
300 % handles    structure with handles and user data (see GUIDATA)
301 % Hint: get(hObject,'Value') returns toggle state of checkbox1
302 global aflag;
303 aflag = 1;
304
305 %
306 % --- Executes on upcheck of checkbox2 for superimposition box.
```

```
348 [legend_h,object_h,plot_h,text_strings] = legend(gca);
349 [n,m]=size(text_strings);
350 counter=m/2;
351 legendname=text_strings;
352 if ishold
353     yes=1;
354 else hold on;
355 end
356 firsttime=0;
357 end
358 fid = fopen(['C:\Documents and Settings\FMBradley\My Documents\Physics\Data Analysis\'  
' , folder, '\Almanac.csv'], 'a');
359 fprintf(fid, '%14.12f %d %d %6.3f %d %6.3f\n', Dalmanac);
360 fclose(fid);
361 if firsttime==1 %print superimposed graphs of row vector data
362 legendname={};
363 legendname=char(legendname);
364 legendname=cellstr(legendname);
365 counter=1;
366 hold on;
367 grid on;
368 firsttime=0;
369 end
370 if flag == 1
371 switch counter
372 case {1}
373 plot(xnplot,ynplot,'og');
374 plot(xinterp,yinterp,'.g');
375 case {2}
376 plot(xnplot,ynplot,'ob');
377 plot(xinterp,yinterp,'.b');
378 case {3}
379 plot(xnplot,ynplot,'oc');
380 plot(xinterp,yinterp,'.c');
381 case {4}
382 plot(xnplot,ynplot,'ok');
383 plot(xinterp,yinterp,'.k');
384 case {5}
385 plot(xnplot,ynplot,'om');
386 plot(xinterp,yinterp,'.m');
387 case {6}
388 plot(xnplot,ynplot,'oy');
389 plot(xinterp,yinterp,'.y');
390 case {7}
391 plot(xnplot,ynplot,'or');
392 plot(xinterp,yinterp,'.r');
393 case {8}
394 plot(xnplot,ynplot,'sg');
395 plot(xinterp,yinterp,'*g');
```

APPENDIX B. IMAGE DATA EXTRACTION ROUTINE (IMAGEDATAMANIPULATOR.M)

C:\Documents and Settings\FMBradley\M...\imagedatamanipulator.m Page 1
November 16, 2005 5:44:29 PM

```
1
2 function [almanacR,almanacC,xnplot,ynplot,xinterp,yinterp,sample_name,BeamEnergy,prob ↵
e_current]=imagedatamanipulator(tiftoload,aflag,gflag,fitflag,folder);
3
4 persistent fileserial;                                     %Allows var fileserial to hold value ↵
for an entire session of multiple calls to this fn
5                                         %if loop tests if variables are being ↵
saved to file,
6                                         %and increments fileserial
7                                         %to help differentiate
8                                         %figures
9 fileserial=fileserial+1;
10 %resets all figures and variables
11 %if ishold
12   % clf;
13   % hold off;
14 %end
15
16 %read in image file
17 I0 = imread (tiftoload);
18 I0 = double(I0);
19 I0(:,1)=0;
20
21 %Initialize variables
22 Test=0;
23 m=0;
24 % Test for location of the spike of interest
25 [Y,I]=max(I0);      %Two vectors: Y=max value of each column, I=Row# of each columns ↵
Max)
26 [K,L]=size(I);      %K=row size, L=column size
27 MinVariance=300;
28 for m=1:(L-26)      %start test sequence at 1 go to length of indice matrix
29   a=25;                %test for remaining testable length less than 25 only take wh ↵
ats left
30   for n=1:a            %Begin creation of test vector. Populate with 25 elements of I (r ↵
ow # of max from each column)
31     Test(n)=I((m+n));
32   end
33   Variance=std(Test); %Calculate variance of max values' row#s to select desired d ↵
ata sample.
34   if Variance < MinVariance  %Update minimum variance
35     MinVariance=Variance;
36     seqstart=m;           %save indice start point in vector I of desired data ↵
sample (row #s of desired data sample)
37     seqstop=m+a;
38     seqlength=a;          %define sequence length to allow for seqlength to be ↵
used as indice addition term for creation of new vector.
39
40 end
```

```
41 end
42 %Test Row data for least variance of column numbers for selected column data sample
43 I0T=I0';
44 [Y2,I3]=max(I0T);           %Two vectors: Y2=max value of each Row, I3=Col# of each row's Max)
45 [KR,LR]=size(I3);
46
47 MinVarianceR=500;
48 a=25;
49 for m3=2:(LR-a-1)          %Loop through all row numbers
50     for n=1:a                %Begin creation of test vector. Populate with 25 elements of I
2 (Column # of max from each row)
51         TestR(n)=I3((m3+n));
52     end
53 VarianceR=std(TestR);       %Calculate variance of maximum values' column #'s to select desired data sample.
54 if VarianceR < MinVarianceR %Update minimum variance
55     MinVarianceR=VarianceR;
56     seqstartR=m3;           %save indice start point in vector I2 of desired data sample (Column #'s of desired data sample)
57     seqstopR=m3+a;
58     seqlengthR=a;           %define sequence length to allow for seqlength to be used as indice addition term for creation of new vector
59 end
60 end
61
62 %Compare MaxValue vectors and choose column and row with largest same maximum
63 PeakPixelValue=0;
64 for stepR=1:25;
65     for stepC=1:25;
66         if Y(stepC+seqstart)==Y2(stepR+seqstartR)
67             Peak=Y(stepC+seqstart);
68             if Peak>PeakPixelValue
69                 PeakPixelValue=Peak;
70                 MaxPixelColNum=seqstart+stepC;
71                 MaxPixelRowNum=seqstartR+stepR;
72             end
73         end
74     end
75 end
76
77 %extract row and column data
78 RowData=I0(MaxPixelRowNum,:);
79 ColData=I0(:,MaxPixelColNum);
80
81 %Create Noise vector from data outside of spike
82 %Calculate variance of noise and through out sample data vectors
83 for z=1:50
84     NoiseData(z)=RowData(z);
```

```
85 end
86
87 RawVarOfNoise=std(NoiseData);
88 RawMeanOfNoise=mean(NoiseData);
89 for z1=1:50
90     if NoiseData(z1) >= RawMeanOfNoise+RawVarOfNoise
91         NoiseData(z1)=RawMeanOfNoise;
92     end
93 end
94 MeanOfNoise=mean(NoiseData);           %Calculate average of noise within variance
95 VarOfNoise=std(NoiseData);
96                               %Normalize row vector of sample data
97 NormRowData=(RowData-MeanOfNoise)/(PeakPixelValue-MeanOfNoise);
98
99                               %Normalize ColData vector
100 for z=1:50
101     NoiseDataCol(z)=ColData(z);
102 end
103
104 RawVarOfNoiseCol=std(NoiseDataCol);
105 RawMeanOfNoiseCol=mean(NoiseDataCol);
106 for z1=1:50
107     if NoiseDataCol(z1) >= RawMeanOfNoiseCol+(2*RawVarOfNoiseCol)
108         NoiseDataCol(z1)=RawMeanOfNoiseCol;
109     end
110 end
111
112 %Calculate average of noise within variance
113 MeanOfNoiseCol=mean(NoiseDataCol);
114 VarOfNoiseCol=std(NoiseDataCol);
115 NormColData=(ColData-MeanOfNoiseCol)/(PeakPixelValue-MeanOfNoiseCol);

116 %add spline interpolation
117 xr= (MaxPixelColNum-49):(MaxPixelColNum+50);
118 xc= (MaxPixelRowNum-49):(MaxPixelRowNum+50);
119 for xl=1:100
120     yr(xl) = NormRowData(MaxPixelColNum-50+xl);
121     yc(xl)=NormColData(MaxPixelRowNum-50+xl);
122 end
123
124 csc = spline(xc,[0 yc 0]);
125 csr=spline(xr,[0 yr 0]);
126 xxr=linspace((MaxPixelColNum-50),(MaxPixelColNum+50),1000);
127 xxc = linspace((MaxPixelRowNum-50),(MaxPixelRowNum+50),1000);
128
129
130 %Extract Halfmaxfullwidth from the normalized Row data
131 maxdif=1;maxdify=1;
132 for xxxx=1:500
```

```
133     dif=abs(0.2-ppval(csr,xxr(xxx)));
134     if dif<maxdif
135         maxdif=dif;
136         lhshalfmax=xxr(xxx);
137     end
138 end
139 for xxy=500:1000
140     dify=abs(0.2-ppval(csr,xxr(xxy)));
141     if dify<maxdify
142         maxdify=dify;
143         rhshalfmax=xxr(xxy);
144     end
145 end
146 hold;
147 Rhalfmaxfullwidth=rhshalfmax-lhshalfmax
148
149 %Extract the halfmaxfullwidth from the normalized column data
150 maxdif=.2;maxdify=.2;
151 for xxx=1:500
152     dif=abs(0.2-ppval(csc,xxc(xxx)));
153     if dif<maxdif
154         maxdif=dif;
155         lhshalfmax=xxc(xxx);
156     end
157 end
158 for xxy=500:1000
159     dify=abs(0.2-ppval(csc,xxc(xxy)));
160     if dify<maxdify
161         maxdify=dify;
162         rhshalfmax=xxc(xxy);
163     end
164 end
165 hold;
166 Chalfmaxfullwidth=rhshalfmax-lhshalfmax;
167
168 %Assign output variables to almanac vector
169 prompt = {'Unique sample name','Enter probe current in "3e-8" notation:','Enter Beam Voltage in format "30" kV:','Enter Exposure Time in "10.005" (sec) format:'};
170 dlg_title = 'Almanac File Definition Input';
171 num_lines= 1;
172 def      = ('S72','6e-10','25','1.0');
173 answer   = inputdlg(prompt,dlg_title,num_lines,def);
174 answerstr=char(answer);
175 sample_name=(answerstr(1,:));
176 probe_current=(answerstr(2,:));
177 BeamEnergystring=(answerstr(3,:));
178 BeamEnergy=str2double(answerstr(3,:));
179 ExpTime=str2double(answerstr(4,:));
180 almanacR=[sample_name str2double(probe_current) 0 BeamEnergy Rhalfmaxfullwidth PeakPi
```

```
    xelValue ExpTime];
181 almanacC=[sample_name str2double(probe_current) 1 BeamEnergy Chalfmaxfullwidth PeakPi
    xelValue ExpTime];
182
183
184
185 % Page 1 graphs. Overview of image with selected max values in colmax/row
186 % and rowmax/col
187 figure(1)
188 title(['Overview page for: ',folder,'_',tiftoload]);
189 subplot(3,1,1), imagesc(abs(I0)); %Shows reproduction of tiff file from MicroCCD
190 hold;
191 plot(MaxPixelColNum,MaxPixelRowNum,'xk');
192 title(['MATLAB reproduction of TIFF (' ,tiftoload, ')']);
193 hold off;
194
195 % Plots maximum per Row vs Column number where that maximum falls in the row.
196 subplot(3,1,2), plot(max(I0));
197 hold;
198 title(['Max Pixel value/Row vs Column Number of MaxPixVal (' ,tiftoload, ')']);
199 plot(MaxPixelColNum,(MeanOfNoise-VarOfNoise),'*y');
200 axis([0,L,(MeanOfNoise-VarOfNoise),(max(Y)+10)]);
201 grid on;
202 hold;
203
204 % Graph Columns' max pixel value vs row Number of MaxpixVal
205 subplot(3,1,3), plot(max(I0T));
206 hold;
207 title(['Max Pixel value/Column vs Row Number of MaxPixVal (' ,tiftoload, ')']);
208 plot(MaxPixelRowNum,(MeanOfNoiseCol-VarOfNoiseCol),'*y');
209 axis([0,LR,(MeanOfNoiseCol-VarOfNoiseCol),(max(Y2)+10)]);
210 grid on;
211 hold;
212
213 %Save figure 1 to file
214 D=now;
215 ddate=day(D);
216 [n,mmmonth]=month(D);
217 dateserial=['_',num2str(ddate),mmmonth,num2str(fileserial)];
218 filetosave=['C:\Documents and Settings\FMBradley\My Documents\Physics\Data Analysis\' ,
    folder,'OV',sample_name,'_',num2str(BeamEnergy),'_',probe_current,dateserial,'.fig'];
219 saveas(1,filetosave);
220
221 %Write NormRowData to file
222 vdatafile=['C:\Documents and Settings\FMBradley\My Documents\Physics\Data Analysis\' ,
    folder,'VRdata_',sample_name,'_',num2str(BeamEnergy),'_',probe_current,dateserial,'.csv'];
```

```
223 fid = fopen(Vdatafile,'w');
224 fprintf(fid,'%11.9f\n',NormRowData);
225 fclose(fid);
226
227 %Write NormColData to file
228 Vdatafile=['C:\Documents and Settings\FMBradley\My Documents\Physics\Data Analysis\', \
229 folder,'VCdata_',sample_name,'_',num2str(BeamEnergy),'_',probe_current,dateserial,'.' \
230 'csv'];
231 fid = fopen(Vdatafile,'w');
232 fprintf(fid,'%11.9f\n',NormColData);
233 fclose(fid);
234
235 %Plot Raw row and column data sets
236 figure(2);
237 title(['Peak plots for: ',folder,'_',tiftoload]);
238 %Raw Row and Column data
239 subplot(2,2,1), plot(RowData,'o');
240 title(['Raw Data for Peak Pixel Row (' ,tiftoload, ')']);
241 axis([(MaxPixelColNum-50),(MaxPixelColNum+50),0,(PeakPixelValue+10)]);
242 grid on;
243 subplot(2,2,2), plot(ColData,'o');
244 title(['Col Data for Peak Pixel Column (' ,tiftoload, ')']);
245 axis([(MaxPixelRowNum-50),(MaxPixelRowNum+50),0,(PeakPixelValue+20)]);
246 grid on;
247
248 %Print Normalized Row Data
249 R=0;xRlimit=0;xRstep=0;
250 [R,xRlimit]=size(NormRowData);
251 for xRstep=1:xRlimit;
252     XRnorm(xRstep)=xRstep-MaxPixelColNum;
253 end
254 subplot(2,2,3), plot(XRnorm,NormRowData,'o');
255 hold;
256 plot((xxr-MaxPixelColNum),ppval(csr,xxr),'.');
257 title(['Normalized Row Data for Peak Pixel Row (' ,tiftoload, ')']);
258 axis([(-50),(50),-.2,1.1]);
259 grid on;
260 text(10,0.5,['FWHM=',num2str(Rhalfmaxfullwidth)]);
261
262
263 %Print Column Data
264 [xlimit,C]=size(NormColData);
265 for xstep=1:xlimit;
266     XCnorm(xstep)=xstep-MaxPixelRowNum;
267 end
268 subplot(2,2,4), plot(XCnorm,NormColData,'o');
269 hold;
```

```
270 plot((xxc-MaxPixelRowNum),ppval(csc,xxc),'.' );
271 title(['Normalized Col Data for Peak Pixel Column (' ,tiftoload, ')']);
272 axis([(-50),(50),-.2,1.1]);
273 grid on;
274 text(10,0.5,['FWHM= ',num2str(Chalfmaxfullwidth)]);
275
276 %Save figure 2 to file
277 filetosave2=['C:\Documents and Settings\FMBradley\My Documents\Physics\Data Analysis\' ,
278 ' ,folder,' \RC_ ',sample_name,' _ ',num2str(BeamEnergy),' _ ',probe_current, dateserial, '. ' ,
279 'fig'];
280 saveas(2, filetosave2);
281
282 %Test for desire for superimposed graph page and set export variables for
283 %consolidation in newfirsttry
284 if (or(gflag,fitflag))
285     xnplot=XRnorm;
286     ynplot=NormRowData;
287     xinterp=xxr-MaxPixelColNum;
288     yinterp=ppval(csx,xxr);
289 else
290     xnplot=0;
291     ynplot=0;
292     xinterp=0;
293     yinterp=0;
294 end
```

THIS PAGE INTENTIONALLY LEFT BLANK

APPENDIX C. LEAST SQUARES FIT ALGORITHM (FBSLD.M)

C:\Documents and Settings\FMBradley\My Documents\Phy...\'fbsLd.m Page 1
November 16, 2005 5:43:45 PM

```
1 %-----Created by FM Bradley to perform a least squares fit for data to the
2 %2-D model for diffusion of minority carriers in a luminscent
3 %semiconductor.
4
5 %Revision Log: 13 September - Time remaining window added by FMBradley
6
7 %Takes a 2-D vector data in (xstepX2) size, normalizes, cuts to 1% of max,
8 %performs a least squares fit to a 2-D model of carrier distro given a
9 %guassian distributed generation area. Output is the fitted model vector,
10 %the difference between model and experimental data, plots of the parameter
11 %space, both curves, the selected of optimal Mu, and n=2sigma radius of
12 %generation area that fits the data.
13
14 function [FittedCurve,residue,Paramspace,Lopt,nopt]=fbsLd(datain,folder,sample_name,BeamEnergy,probe_current)
15
16 %CreateStruct.WindowStyle='replace';
17 % CreateStruct.Interpreter='tex';
18 % h=msgbox('Calculating.....','Progress Monitor',CreateStruct);
19 nmint=le-4      %Significant radius of generation volume distribution(cm) 95% of current ring??
20 V=0;           %Applied bias (Volts)
21 ttau=4.32e-9;   %input variable. Lifetime of carrier in question (s)
22 icd=1.0;        %inter-contact distance (mm) for calculation of electric field associated with V
23 E=V/icd*10;    %Electric field (V/cm)
24 step=0.04e-4;    %step size in (cm)designed to fit the increment size of our experimental data w/interpolation
25 [R3,I3]=size(datain);          %Id dimension of datain array
26 datain(:,1)=0.4e-4.*datain(:,1); %Use this line if the data is coming from actual experimentally gathered and spline interpreted data from the MATLAB GUI.
27                                     %Necessary because spline data is already in microns and we must convert all numbers here to cm
28 Lmin=SlopeL2(datain)-.3e-4;          %Conducts ln slope analysis method for the diffusion length assessment
29 Lstep=.1e-4;
30 stop=0;
31 while (stop<3)
32     switch stop
33         case 0
34             Lstep=.2e-4;
35             nstep=.2e-4;
36             Lmax=Lmin+.4e-4;
37             nmax=nmint+.4e-4;
38         case 1
39             Lstep=.1e-4;
40             nstep=.1e-4;
41             Lmax=Lmin+.2e-4;
```

```
42           nmax=nmin+.2e-4;
43       case 2
44           Lstep=.1e-4;
45           nstep=.1e-4;
46           nmin=nmin-.5e-4;
47           Lmin=Lmin-.5e-4;
48           Lmax=Lmin+1e-4;
49           nmax=nmin+1e-4;
50       end
51
52       a=0;           %step variable for indexing x
53       b=0;           %step variable for indexing y
54       MinSum=10000;
55       istep=0;
56       Paramspace=0;
57       for L=Lmin:Lstep:Lmax
58           t0=cputime;
59           n=nmin;                                %1-d spot dimension of a square
60           istep=istep+1;                          %parameter space indexing variable
61           mu=0;                                  %table for mu
62           jstep=0;                                %param space index variable for mu
63           or n
64           S=(E*L^2)/.025;                         %Field effect (cm)
65           mtproduct=L^2/.025;                     %mu tau product in (cm^2/V)
66           for n=nmin:nstep:nmax
67               G=2/n;                                %Gaussian 2sigma radius
68           or 95% generation distro (unitless)
69               jstep=jstep+1;
70               xmin=datain(1,1);                   %convert datain from pixels to cm dependent upon resolution size of SEM/Optical scope .4microns/pixel
71               xmax=max(datain(:,1));
72               x=xmin;                                % (cm)
73               ymin=0;                                % (cm)
74               ymax=0;                                % (cm)
75               y=ymin;
76               b=0;
77               for yl=ymin:step:ymax
78                   a=0;
79                   b=b+1;
80                   for xl=xmin:step:xmax
81                       Integrand=0;
82                       a=a+1;
83                       Integrand=dblquad(@Intgrnd,(xl-n),(xl+n),(yl-n),(yl+n),step,[],xl,yl,S,L,G);
84                       if (isnan(Integrand)) Integrand=OldIntegrand+.01*OldIntegrand;
```

```
82         end
83         OldIntegrand=Integrand;
84         Int(a,b,1)=x1;
85         Int(a,b,2)=y1;
86         Int(a,b,3) = (G/(2*pi^2*L^2))*Integrand;
87     end    %end x loop
88 end    %end y loop
89 %Least square computation
90 [M2,I2]=max(Int(:,1,3));
91 NormInt=[Int(:,1,1) (Int(:,1,3)./M2)];
92 %LogNormInt=log(NormInt(:,2));
93 %LogDataIn=log(normdatain(:,2));
94 LS=0;
95
96 for loopc=1:R3;                                %1:((dimofdata-1)/2)-105);      ✓
97 %start loop at max +13 and count to end testing for least squares diff
98 %LS(loopc)=(LogNormInt(I2+100+loopc)-LogDataIn(I3+100+loopc))^2
99 %; Used to calculate log difference squares between two lines
100 %of data
101 if isnan(NormInt(loopc,2))
102     NormInt(loopc,2)=1;
103 end
104 if isnan(datain(loopc,2))
105     datain(loopc,2)=1;
106 end
107 if datain(loopc,2)<.7                         %Eliminates t ✓
108     he top 30% of the curve that does not fit our assumptions
109     LS(loopc)=(NormInt(loopc,2)-datain(loopc,2))^2;
110 end                                              %ends non mod ✓
111 el fit data
112 end                                              %ends Least s ✓
113 quares sum loop
114     LoopSum=sum(LS);
115     Paramspace(istep,jstep,1)=(istep-1)*Lstep+Lmin;
116     Paramspace(istep,jstep,2)=(jstep-1)*nstep+nmin;
117     Paramspace(istep,jstep,3)=LoopSum;
118     if LoopSum<MinSum
119         MinSum=LoopSum;
120         residue=MinSum;
121         ModelFit=NormInt;
122         %Muopt=mu;
123         nopt=n;
124         Lopt=L;
125         imin=istep;
126         jmin=jstep;
127     end
128     figure(7);                                  %Plot the search space each round of calc ✓
129     ulations complete
130     nplot=n*1e4;
```

```
126         Lplot=L*1e4;
127         if (stop==1)plot(Lplot,nplot,'xr');
128         else plot(Lplot,nplot,'xk');
129         end
130         if not(ishold) hold;
131         end
132     end                                %end of n for loop
133     % CreateStruct.WindowStyle='replace';
134     % CreateStruct.Interpreter='tex';
135     % h=msgbox(['Total time remaining= ',num2str((cputime-t0)/60)*(Lmax-L)/Lstep),' minutes. Step ',int2str(istep*jstep),' of ',num2str(((Lmax-Lmin)/Lstep)+1)*((nmax-nmin)/nstep+1),' Total Steps'],'Progress Monitor',CreateStruct);
136 end                                    %end of L for loop
137
138 %Decision tree for creating direction of propagation of parameter space
139 %build up.
140 switch imin
141   case 1
142     Lmin=Lmin-Lstep;
143     if jmin==1
144       nmin=nmin-nstep;
145     elseif jmin==2
146       nmin=nmin;
147     else nmin=nmin+nstep;
148     end
149   case 2
150     Lmin=Lmin;
151     if jmin==1
152       nmin=nmin-nstep;
153     elseif jmin==3
154       nmin=nmin+nstep;
155     else
156       stop=stop+1;
157       plot((Lmin*1e4),(nmin*1e4),'xb');
158     end
159   case 3
160     Lmin=Lmin+Lstep;
161     if jmin==1
162       nmin=nmin-nstep;
163     elseif jmin==2
164       nmin=nmin;
165     else nmin=nmin+nstep;
166     end
167   otherwise
168     break;
169   end                                %end for the switch loop
170 end                                    %end for the while loop
171 title('Search Space');               %Label Figure 7
172 xlabel('Ld (\mu m)');
```

```
173     ylabel('2\sigma (\mu)');
174 hold; %Hold off for figure 7
175 FittedCurve=ModelFit;
176 %Write Fitted Curve data to file
177 Vdatafile=['C:\Documents and Settings\FMBradley\My Documents\Physics\Data Analysis\',  
    folder,'\'ModelFit',sample_name,'Ld_',Lopt,'_',num2str(BeamEnergy),'kv_',probe_current,  
,'.csv']
178 fid = fopen(Vdatafile,'w');
179 fprintf(fid,'%11.9f\n',ModelFit);
180 fclose(fid);
181 Residue=MinSum
182 nopt
183 Lopt
184
185
186 %plot the resulting fitted curves
187 figure(8);
188 plot(ModelFit(:,1),ModelFit(:,2),'.b',datain(:,1),datain(:,2),'-r');
189 hold on;
190 Xmax=xmax;
191 Xmin=xmin;
192 Ymin=0;
193 Ymax=1.0;
194 Axis([Xmin Xmax Ymin Ymax]);
195 title('Normalized Experimental vs. Model Fit');
196 xlabel('Radial distance from beam center (cm)');
197 ylabel('Normalized Intensity');
198 %'\mu: \mu_0=',num2str(Muopt),':\tau=',num2str(tau*1e9),
199 legendname1=['Model Fit: (n=',num2str(nopt*1e4),'\mu: Ld=',num2str(Lopt*1e4),'\mu) R  
esidue=',num2str(residue)];
200 legendname2=['Data: ',sample_name,:PC=,num2str(probe_current), 'Amps'];
201 legend(legendname1,legendname2);
202 hold off;
203
204
205 %Plot the parameter space of the resulting 1Micronx1Micron parameter range for both 2  
sigma and Ld
206 figure(9);
207 contour(Paramspace(:,:,2),Paramspace(:,:,1),Paramspace(:,:,3),100);
208 hold on;
209 plot(nopt,Lopt,'*y')
210 Xmax=nmax;
211 Xmin=nmin;
212 Ymin=Lmin;
213 Ymax=Lmax;
214 Axis([Xmin Xmax Ymin Ymax]);
215 title(['Parameter Space: ',sample_name,':',num2str(BeamEnergy),':kv:',num2str(probe_cu  
rrent),':A']);
216 ylabel('Ld step multiples [cm^2/Vs]');
```

```
217 xlabel('2\sigma steps of generation area [cm]');
218 colorbar('vert');
219 hold off;
```

APPENDIX D. VECTOR DATA EXTRACTION ROUTINE "VDATAMANIPULATOR.M"

```
C:\Documents and Settings\FMBradley\My Do... \vdatamanipulator.m      Page 1
November 16, 2005          5:46:14 PM


---


1 function [almanacV,xnplot,ynplot,xinterp,yinterp,sample_name,BeamEnergy,probe_current] = vdatamanipulator(filetoload,aflag1,gflag1,dirname);
2
3 persistent fileserial;                                %Allows var fileserial to hold value ✓
4 for an entire session of multiple calls to this fn
5                                         %if loop tests if variables are being ✓
6                                         saved to file,
7                                         %and increments fileserial
8                                         %to help differentiate
9                                         %figures
10 fileserial=fileserial+1;
11
12 %resets all figures and variables
13 %if ishold
14   % clf;
15   % hold off;
16   %end
17 %Row data input manipulation loop
18 %filename=input('Enter row data file name:','s');
19 rowdatainput=load(filetoload);
20 RowData=rowdatainput(:,2);
21
22 %Data preparation loop
23 [PeakPixelValue,MaxPixelColNum]=max(RowData);
24
25 %Create Noise vector from data outside of spike
26 %Calculate variance of noise and through out sample data vectors
27 for z=1:200
28   NoiseData(z)=RowData(z);
29 end
30
31 RawVarOfNoise=std(NoiseData);
32 RawMeanOfNoise=mean(NoiseData);
33 for z1=1:200
34   if NoiseData(z1) >= RawMeanOfNoise+RawVarOfNoise
35     NoiseData(z1)=RawMeanOfNoise;
36   end
37 end
38 MeanOfNoise=mean(NoiseData);           %Calculate average of noise within variance
39 VarOfNoise=std(NoiseData);            %Normalize row vector of sample data
40 NormRowData=(RowData-MeanOfNoise)/(PeakPixelValue-MeanOfNoise);
41
42 %add spline interpolation
43 xr= (MaxPixelColNum-49):(MaxPixelColNum+50);
44 for xl=1:100
45   yr(xl) = NormRowData(MaxPixelColNum-50+xl);
46 end
```

```
47      csr=spline(xr,[0 yr 0]);
48      xxr=linspace((MaxPixelColNum-50),(MaxPixelColNum+50),1000);
49
50 %Extract Halfmaxfullwidth from the normalized Row data
51 maxdif=1;maxdify=1;
52 for xxx=1:500
53     dif=abs(0.2-ppval(csr,xxr(xxx)));
54     if dif<maxdif
55         maxdif=dif;
56         lhshalfmax=xxr(xxx);
57     end
58 end
59 for xxy=500:1000
60     dify=abs(0.2-ppval(csr,xxr(xxy)));
61     if dify<maxdify
62         maxdify=dify;
63         rhshalfmax=xxr(xxy);
64     end
65 end
66 Rhalfmaxfullwidth=rhshalfmax-lhshalfmax;
67
68 %Assign output variables to almanac vector
69 prompt = {'Unique sample name','Enter probe current in "3e-8" notation:','Enter Beam Voltage in format "30" kV:','Enter Exposure Time in "10.005" (sec) format:','Enter R or C for Row or Column Data'};
70 dlg_title = 'Almanac File Definition Input';
71 num_lines= 1;
72 def      = {'S72','6e-10','25','1.0','R'};
73 answer   = inputdlg(prompt,dlg_title,num_lines,def);
74 answerstr=char(answer);
75 sample_name=(answerstr(1,:));
76 probe_current=(answerstr(2,:));
77 BeamEnergystring=(answerstr(3,:));
78 BeamEnergy=str2double(answerstr(3,:));
79 ExpTime=str2double(answerstr(4,:));
80 switch answerstr(5)
81     case 'R'
82         vector_type='0';
83     case 'C'
84         vector_type='1';
85     otherwise
86         dialog('Your test did not work');
87 end
88 almanacV=[str2double(probe_current) vector_type BeamEnergy Rhalfmaxfullwidth PeakPixelValue ExpTime];
89
90 %Analysis output loop
91 %Plot Raw row and column data sets
92 figure(1);
```

```
93 %Plot overview graph of row
94 subplot(1,2,1), plot(RowData,'o');
95 title(['Raw Data for Peak Pixel Vector (',foldername,filetoload,')']);
96 axis([(MaxPixelColNum-50),(MaxPixelColNum+50),0,(PeakPixelValue+10)]);
97 grid on;
98
99 %Print Row Data
100 [xRlimit,R]=size(NormRowData);
101 for xRstep=1:xRlimit;
102     XRnorm(xRstep)=xRstep-MaxPixelColNum;
103 end
104 subplot(1,2,2), plot(XRnorm,NormRowData,'o');
105 hold;
106 plot((xxr-MaxPixelColNum),ppval(csr,xxr),'.');
107 title(['Normalized Data for Peak Pixel Vector (',filetoload,')']);
108 axis([-50,50,-.2,1.1]);
109 grid on;
110 text(10,0.5,['FWHM=',num2str(Rhalfmaxfullwidth)]);
111 hold;
112
113 %Save figure 1 to file
114 D=now;
115 ddate=day(D);
116 [n,mmmonth]=month(D);
117 dateserial=['_',num2str(ddate),mmmonth,num2str(fileserial)];
118 filetosave=['C:\Documents and Settings\FMBradley\My Documents\Physics\Data Analysis\' ↵
, foldername, '\',answerstr(4),num2str(BeamEnergy), '_',probe_current,dateserial,'.fig'] ↵
;
119 saveas(1,filetosave);
120 figure(2);
121
122 %Set export variables for
123 %consolidation in newfirstry
124     xnplot=XRnorm;
125     ynplot=NormRowData;
126     xinterp=xxr-MaxPixelColNum;
127     yinterp=ppval(csr,xxr);
```

THIS PAGE INTENTIONALLY LEFT BLANK

APPENDIX E. SLOPE ANALYSIS ALGORITHM (SLOPEL2.M)

C:\Documents and Settings\FMBradley\My Documents\P...\SlopeL2.m Page 1
November 16, 2005 5:45:34 PM

```
1 function [L]=SlopeL(datavector)
2 %
3 %
4 %-----Automated slope determination algorithm
5 %to gain initial indication of diffusion length of a material.
6 % Original protocol determined by Dave Luber. Automated by Mitch Bradley
7 % 3 October, 2005
8 j=1;
9 y=0;
10 i=1;
11 [V,I]=max(datavector(:,2));
12 EOY=size(datavector(:,1));
13 for i=1:I
14 y=datavector(i,2);
15 if(y<.1) %These limits should be adjusted for noise level of the sample image (ZOOM above lower limit)
16 if (y>.01) %This should be adjusted for lower limit of noise level
17 l for sample image
18 yfit(j)=log(y);
19 xfit(j)=datavector(i,1);
20 j=j+1;
21 end
22 %i=i+1;
23 end
24 p=polyfit(xfit,yfit,1); %conduct polylinomial fit for poly of degree 1 (linear) for data in xfit and yfit
25 L=1/p(1)
26 b=p(2)
27 fitdata=[xfit', yfit'];
28
29 % _____ Loop for the right side of the distribution _____
30 j=1;
31 for i=I:EOY
32 yr=datavector(i,2);
33 if(yr<.1) %These limits should be adjusted for noise level of the sample image (ZOOM above lower limit)
34 if (yr>.01) %This should be adjusted for lower limit of noise level
35 el for sample image
36 yfitr(j)=log(yr);
37 xfitr(j)=datavector(i,1);
38 j=j+1;
39 end
40 %i=i+1;
41 end
42 pr=polyfit(xfitr,yfitr,1); %conduct polylinomial fit for poly of degree 1 (linear) for data in xfit and yfit
```

```
43 Lr=-1/pr(1)
44 br=pr(2)
45 fitdataR=[xfitr', yfitr'];
46
47 %-----Plot ln(Intensity) vs X pos for all data left of spot-----
48 figure(4);
49 plot(datavector(:,1),log(datavector(:,2)));
50 %axis([(datavector(1,1)),(0),(log(min(datavector(:,2)))),(0)]);
51 title('LN(Intensity) of Left Side Distribution');
52 xlabel('Radial distance from beam center (cm)');
53 ylabel('LN(Normalized Intensity)');
54
55 %-----Calculate error reports and plot line slopes-----
56 figure(5);
57 Lplus=L+(.4e-4)/(max(yfit)-yfit(1));           %The Plus factor should be .4e-4 for ↵
      real data and .04e-4 for tfbs control data
58 Lminus=L-(.4e-4)/(max(yfit)-yfit(1));          %The minus factor should be .4e-4 for ↵
      real data and .04e-4 for tfbs control data
59 plot(xfit,yfit,'ob');
60 hold;
61 plot(xfit,polyval(p,xfit),'-r');
62 yplus=(1/Lplus)*xfit+b;
63 yminus=(1/Lminus)*xfit+b;
64 plot(xfit,yplus,'-g');
65 plot(xfit,yminus,'-k');
66 %                                     Right side_
67 Lplusr=Lr+(.4e-4)/(max(yfitr)-min(yfitr));      %The Plus factor should be .4e-4 for ↵
      4 for real data and .04e-4 for tfbs control data
68 Lminusr=Lr-(.4e-4)/(max(yfitr)-min(yfitr));      %The minus factor should be .4e-4 for ↵
      -4 for real data and .04e-4 for tfbs control data
69 plot(xfitr,yfitr,'ob');
70 plot(xfitr,polyval(pr,xfitr),'-r');
71 yplusr=(-1/Lplusr)*xfitr+br;
72 yminusr=(-1/Lminusr)*xfitr+br;
73 plot(xfitr,yplusr,'-g');
74 plot(xfitr,yminusr,'-k');
75
76 legendname1=['Data Points'];
77 legendname2=['L actual Ld=',num2str(L*1e4), '\u03bc'];
78 legendname3=['L Ld(+)=',num2str(Lplus*1e4), '\u03bc'];
79 legendname4=['L Ld(-)=',num2str(Lminus*1e4), '\u03bc'];
80 legendname5=['Data Points'];
81 legendname6=['R actual Ld=',num2str(Lr*1e4), '\u03bc'];
82 legendname7=['R Ld(+)=',num2str(Lplusr*1e4), '\u03bc'];
83 legendname8=['R Ld(-)=',num2str(Lminusr*1e4), '\u03bc'];
84
85
86 legend(legendname1,legendname2,legendname3,legendname4,legendname5,legendname6,legend ↵
      name7,legendname8);
```

```
87 title('Slope Analysis Estimate of Ld');  
88 xlabel('Radial distance from beam center (cm)');  
89 ylabel('LN(Normalized Intensity)');  
90 hold;  
91
```

THIS PAGE INTENTIONALLY LEFT BLANK

APPENDIX F. NUMERICAL INTEGRATION SOLUTION FOR MINORITY CARRIER DISTRIBUTION (INTEGRAND.M)

C:\Documents and Settings\FMBradley\My Documents\P...\Intgrnd.m Page 1
November 16, 2005 5:45:03 PM

```

1 function I=Intgrnd(chi,ada,x1,y1,S,L,G)
2 I=exp(-(G^2).*((x1-chi).^2+(y1-ada).^2)+(S.*chi/(2*L.^2))).*besselk(0,(sqrt((S.^2+4*L.^2).*((chi.^2+ada.^2))/(2*L.^2)));
3 %I=exp(S.*chi/(2*L.^2)).*besselk(0,(sqrt(S.^2+4*L.^2).*((chi.^2+ada.^2).^(.5)/(2*L.^2));
4 );

```

THIS PAGE INTENTIONALLY LEFT BLANK

APPENDIX G. PHOTON RECYCLING PERTURBATION

REFERENCE EQUATION SHEET

Calculated Properties	Measured Properties	Referenced Properties
$T_{\text{radiation}} := \frac{1}{210^{10} Na}$	$Na = 4 \cdot 10^{-19}$	$\alpha := 4$
	$Lm = 4$	$\theta := 1.21 R1 := 0.001$
	$Lw := \frac{1}{\alpha} = 2.542 \cdot 10^{-4}$	$\Omega := 1.21 R2 := 0.001$
	$t := 1$	$w := 1 \cdot 10^{-4}$
	$R(a, \theta) := \int_1^{\infty} \frac{e^{-xt}}{t^n} dt$	$Dm := \frac{Lm}{t} = 2.542 \cdot 10^{-4}$
	$T0 := \frac{\left[-2H(3\alpha \frac{w}{\cos(\theta)}) + H(3.2\alpha \frac{w}{\cos(\theta)}) + \frac{1}{2} \right] + \left[1 + \left(H(3\alpha w) + H(3.2\alpha w) + \frac{1}{2} \right) \frac{R2 \cdot R1}{2 \cdot \alpha \cdot w} + \left(\frac{\cos(\theta)^2 - 1 - R1}{\alpha \cdot w} \right) \left(-2H(3\alpha \frac{w}{\cos(\theta)}) + H(3.2\alpha \frac{w}{\cos(\theta)}) + \frac{1}{2} \right) \right]}{2 \cdot \alpha \cdot w t}$	$\alpha := 4$
	$T0 := \left[\left(\frac{1}{t} + T0 \right) \right]^{-1}$	$w := 1 \cdot 10^{-4}$
$T2 := \left(\frac{1}{tw} \right)$	$Da := Dm \cdot T2$	$Lm = \sqrt{Dm}$
	$Da := 1$	$Lw = 1$
	$\mu := \frac{Da}{.025}$	$\mu = 1$

SAMPLE D6

Calculated Properties	Measured Properties	Referenced Properties
$T_{\text{radiation}} := \frac{1}{210^{10} Na}$	$Na = 3.5 \cdot 10^{-19}$	$\alpha := 3500$
	$Lm = 1.21 \cdot 10^{-4}$	$\theta := 1.21 R1 := 0.001$
	$t := 1.429 \cdot 10^{10}$	$\Omega := 1.21 R2 := 0.001$
	$Lw := \frac{1}{\alpha} = 2.852 \cdot 10^{-4}$	$w := 1 \cdot 10^{-4}$
	$R(a, \theta) := \int_1^{\infty} \frac{e^{-xt}}{t^n} dt$	$Dm := \frac{Lm}{t} = 151.579$
	$T0 := \frac{\left[-2H(3\alpha \frac{w}{\cos(\theta)}) + H(3.2\alpha \frac{w}{\cos(\theta)}) + \frac{1}{2} \right] + \left[1 + \left(H(3\alpha w) - \frac{1}{2} \right) \frac{1}{\alpha \cdot w} + \left(-2H(3\alpha w) + H(3.2\alpha w) + \frac{1}{2} \right) \frac{R2 \cdot R1}{2 \cdot \alpha \cdot w} + \left(\frac{\cos(\theta)^2 - 1 - R1}{\alpha \cdot w} \right) \left(-2H(3\alpha \frac{w}{\cos(\theta)}) + H(3.2\alpha \frac{w}{\cos(\theta)}) + \frac{1}{2} \right) \right]}{2 \cdot \alpha \cdot w t}$	$\alpha := 3500$
	$T0 := \left[\left(\frac{1}{t} + T0 \right) \right]^{-1}$	$w := 6.8 \cdot 10^{-11}$
$T2 := \left(\frac{1}{tw} \right)$	$Da := Dm \cdot T2$	$Lm = \sqrt{Dm}$
	$Da := 150.297$	$Lw = 1.016 \cdot 10^{-4}$
	$\mu := \frac{Da}{.025}$	$\mu = 6.012 \cdot 10^0$

SAMPLE E3

Calculated Properties	Measured Properties	Referenced Properties
$T_{\text{radiation}} := \frac{1}{210^{10} Na}$	$Na = 4 \cdot 10^{-19}$	$\alpha := 3400$
	$Lm = 1.4 \cdot 10^{-4}$	$\theta := 1.21 R1 := 0.001$
	$t := 1.40 \cdot 10^{12}$	$\Omega := 1.21 R2 := 0.001$
	$Lw := \frac{1}{\alpha} = 2.944 \cdot 10^{-4}$	$w := 1 \cdot 10^{-4}$
	$R(a, \theta) := \int_1^{\infty} \frac{e^{-xt}}{t^n} dt$	$Dm := \frac{Lm}{t} = 140$
	$T0 := \frac{\left[-2H(3\alpha \frac{w}{\cos(\theta)}) + H(3.2\alpha \frac{w}{\cos(\theta)}) + \frac{1}{2} \right] + \left[1 + \left(H(3\alpha w) - \frac{1}{2} \right) \frac{1}{\alpha \cdot w} + \left(-2H(3\alpha w) + H(3.2\alpha w) + \frac{1}{2} \right) \frac{R2 \cdot R1}{2 \cdot \alpha \cdot w} + \left(\frac{\cos(\theta)^2 - 1 - R1}{\alpha \cdot w} \right) \left(-2H(3\alpha \frac{w}{\cos(\theta)}) + H(3.2\alpha \frac{w}{\cos(\theta)}) + \frac{1}{2} \right) \right]}{2 \cdot \alpha \cdot w t}$	$\alpha := 3400$
	$T0 := \left[\left(\frac{1}{t} + T0 \right) \right]^{-1}$	$w := 8.538 \cdot 10^{-11}$
$T2 := \left(\frac{1}{tw} \right)$	$Da := Dm \cdot T2$	$Lm = \sqrt{Dm}$
	$Da := 138.55$	$Lw = 1.088 \cdot 10^{-4}$
	$\mu := \frac{Da}{.025}$	$\mu = 5.542 \cdot 10^0$

SAMPLE F4

Calculated Properties	Measured Properties	Referenced Properties
$\tau_{\text{radiation}} := \frac{1}{216 \cdot 10^6 \cdot \text{Na}}$	$\text{Na} = 6 \cdot 10^{-9}$ $L = 1.8 \cdot 10^{-4}$ $t = 8.33 \cdot 10^{11}$	$\alpha = 3000$ $\theta = 1.21 \cdot R = .001$
$R = \frac{1}{\alpha} = 3.33 \cdot 10^{-4}$		$R2 = 1.21 \cdot R2 = .001$ $w = 10^{-9}$
$R(a, z) := \int_1^{\infty} \frac{e^{-xt}}{t^n} dt$	$Dm = \frac{\text{Lm}^2}{\tau}$	$Dm = 193.966$
$T0 = \frac{\left[-3H(3\alpha - \frac{w}{\cos(\theta)}) + H(3.2\alpha - \frac{w}{\cos(\theta)}) + \frac{1}{2} \right] + \left[-2H(3\alpha w) + H(3.2\alpha w) + \frac{1}{2} \right] \frac{R2 \cdot R1}{2\alpha w} + \left(-2H(3\alpha - \frac{w}{\cos(\theta)}) + H(3.2\alpha - \frac{w}{\cos(\theta)}) + \frac{1}{2} \right)}{t}$ $T0 = 6.626 \cdot 10^0$ $w = \left[\frac{1}{t} \right] + (T0)^{-1}$ $w = 6.559 \cdot 10^{11}$		
$T2 = \left(\frac{1}{tw} \right) \left[\frac{\left[\frac{\cos(\theta)^2 \left(-2H(5\alpha - \frac{w}{\cos(\theta)}) + H(5.2\alpha - \frac{w}{\cos(\theta)}) + \frac{1}{4} \right) + H(3\alpha - \frac{w}{\cos(\theta)}) \frac{w^2}{\alpha} \right]}{2a} + \left(-2H(5\alpha w) + H(5.2\alpha w) + \frac{1}{4} \right) \frac{R2 \cdot R1}{2\alpha w} + \left(-2H(3\alpha - \frac{w}{\cos(\theta)}) + H(3.2\alpha - \frac{w}{\cos(\theta)}) + \frac{1}{2} \right)}{(1-R) \cdot \cos(\theta)^2} \right] + \left(-2H(3\alpha w) + H(3.2\alpha w) + \frac{1}{4} \right) \frac{(R2 \cdot R1) \left[H(3 \cdot w) \left(\frac{w^2}{\alpha} \right) + \frac{1}{3} \right]}{2} + \frac{3 \left(H(5 \cdot w) \frac{1}{4} \right)}{a^3} + \frac{w \left(2H(4\alpha w) + \frac{1}{2} \right)}{a^2}$	$Dm = Dm - T2$ $Dm = 191.89$ $\mu := \frac{Da}{.025}$	$L = \sqrt{Dm}$ $L = 1.122 \cdot 10^{-4}$ $\mu = 7.676 \cdot 10^3$

SAMPLE G8

Calculated Properties	Measured Properties	Referenced Properties
$\tau_{\text{radiation}} := \frac{1}{216 \cdot 10^6 \cdot \text{Na}}$	$\text{Na} = 1 \cdot 10^{-9}$ $L = 1.0 \cdot 10^{-4}$ $t = 5 \times 10^{11}$	$\alpha = 2300$ $\theta = 1.21 \cdot R = .001$
$R = \frac{1}{\alpha} = 4.348 \cdot 10^{-4}$		$R2 = 1.21 \cdot R2 = .001$ $w = 10^{-9}$
$R(a, z) := \int_1^{\infty} \frac{e^{-xt}}{t^n} dt$	$Dm = \frac{\text{Lm}^2}{\tau}$	$Dm = 909.091$
$T0 = \frac{\left[-3H(3\alpha - \frac{w}{\cos(\theta)}) + H(3.2\alpha - \frac{w}{\cos(\theta)}) + \frac{1}{2} \right] + \left[-2H(3\alpha w) + H(3.2\alpha w) + \frac{1}{2} \right] \frac{R2 \cdot R1}{2\alpha w} + \left(-2H(3\alpha - \frac{w}{\cos(\theta)}) + H(3.2\alpha - \frac{w}{\cos(\theta)}) + \frac{1}{2} \right)}{t}$ $T0 = 1.019 \cdot 10^0$ $w = \left[\frac{1}{t} \right] + (T0)^{-1}$ $w = 9.894 \cdot 10^{12}$	$Dm = Dm - T2$ $Dm = 906.004$ $\mu := \frac{Da}{.025}$	$L = \sqrt{Dm}$ $L = 9.466 \cdot 10^{-5}$ $\mu = 3.624 \cdot 10^0$
$T2 = \left(\frac{1}{tw} \right) \left[\frac{\left[\frac{\cos(\theta)^2 \left(-2H(5\alpha - \frac{w}{\cos(\theta)}) + H(5.2\alpha - \frac{w}{\cos(\theta)}) + \frac{1}{4} \right) + H(3\alpha - \frac{w}{\cos(\theta)}) \frac{w^2}{\alpha} \right]}{2a} + \left(-2H(5\alpha w) + H(5.2\alpha w) + \frac{1}{4} \right) \frac{R2 \cdot R1}{2\alpha w} + \left(-2H(3\alpha - \frac{w}{\cos(\theta)}) + H(3.2\alpha - \frac{w}{\cos(\theta)}) + \frac{1}{2} \right)}{(1-R) \cdot \cos(\theta)^2} \right] + \left(-2H(3\alpha w) + H(3.2\alpha w) + \frac{1}{4} \right) \frac{(R2 \cdot R1) \left[H(3 \cdot w) \left(\frac{w^2}{\alpha} \right) + \frac{1}{3} \right]}{2} + \frac{3 \left(H(5 \cdot w) \frac{1}{4} \right)}{a^3} + \frac{w \left(2H(4\alpha w) + \frac{1}{2} \right)}{a^2}$		

LIST OF REFERENCES

1. Sze, SM. *Semiconductor Devices*. Wiley&Sons, 2002.
2. Bolognesi, C.R. et al. *Appl. Phys. Lett.* **86**, 253506-1-3, (2005).
3. Crowe, T.W., et al., "GaAs Schottky diodes for THz mixing applications," *Proc. IEEE.* **80**, 1827, (Nov 1992).
4. Jae-Sung Rieh, et al. *IEEE Transactions on Microwave Theory and Techniques*. **52**, no. 10, (Oct 2004).
5. Woodall, J. et al. "An InAs Based Transistor Approach to Terahertz Electronics including Improved GaAlAs/GaAs HBTs." [electronic bulletin board for research laboratory] (cited 6 Dec, 2005); available at http://www.eng.yale.edu/faculty/vita/Woodall_lab.htm
6. Haegel, N.M., Fabbi, J.D. and Coleman, M.P., *Appl. Phys. Lett.* **84**, 1329 (2004).
7. Haegel, N.M., D.R. Luber, F.M. Bradley, M. Talmadge and M.P. Coleman. "Imaging Transport for the Determination of Minority Carrier Diffusion Length." submitted to *Review of Scientific Instruments*, September 2005.
8. Luber, D.R., Bradley, F.M. and Haegel, N.M., "Imaging Transport for the Determination of Minority Carrier Diffusion Length." submitted to *Appl. Phys. Lett.*, August 2005
9. Lowney, J.R., Bennett, H.S., *J. Appl. Phys.* **69**, (10), 7102, (1991).

10. DARPA, Broad Agency Announcement 99-15 "Terahertz Technology for Sensing and Satellite Communications" from the *Commerce Business Daily*, Issue No. 2243, 1998.
11. Brisar, John, "Light Emitting Polymers on Flexible Substrates for Naval Firefighting Applications". Master's Thesis, Naval Postgraduate School, 2005.
12. Yacobi, B. G. and D. B. Holt, *Cathodoluminescence Microscopy of Inorganic Solids*, (Plenum, New York, 1990), p. 59 and references therein.
13. Kayana, K. and Okayama, S., *J. Appl. Phys.* **5**, 43 (1972).
14. Talmadge, M., Internal Haegel laboratory Report. July, 2005.
15. Donolato & Venturi, "Influence of Generation Distribution on the Calculated EBIC Contrast of Line Defects", *Phy. Stat. Sol.(a)*, **78**, 377 (1982).
16. Arfken, G.B, Weber, H.J., *Mathematical Methods for Physicists*. (Academic Press, San Diego, CA, 2001), pg. 554.
17. Freeman, Will. "Imaging Transport: Optical Measurements of Diffusion and Drift in Semiconductor Materials and Devices." Master's Thesis, Naval Postgraduate School, September, 2004.
18. Possin, G.E. & Norton, J.F., *Scanning Electron Microscopy 1975*, (IIT Res. Inst. Chicago, 1975), pg. 475.

19. Luber, DR & Haegel, NM. "Direct Imaging of Electron Beam Interaction Region," submitted for review Appl. Phys. Lett., 2005.
20. Goldstein, Joseph, et al. *Scanning Electron Microscopy and X-Ray Microanalysis, Third Edition* (Plenum, New York, 2002).
21. Everhart, E., Herzog, R.F., Chang,M.S. and DeVore, W.J. In *Proceedings of the 6th International Conference on X-Ray Optics and Microanalysis* (G. Shinoda, K. Kohra and T. Ichinokawa, eds.), (University of Tokyo Press, Tokyo, 1972). p. 81.
22. Boone, Tom. "High-Speed Optical Modulation Techniques incorporating heavy p-type doping and lateral drift developed in Gallium Arsenide." PHD Dissertation, Yale University. May, 2004.
23. Bennett, H. S., *J. Appl. Phys.* **92**, 8 (2002).
24. Harmon, E.S., Lovejoy, M.L., Melloch, M.R. and Lundsfrom, M.S., "Experimental observations of a minority electron mobility enhancement in degenerately doped p-type GaAs," *Appl.Phys.Lett.* **63**, (4), (1993).
25. Kim, D.M., et al., *J. Appl. Phys.* **69**, 7102 (1991).
26. Lovejoy, M.L., et al., *Appl. Phys. Lett.* **61**, 822 (1992).
27. Furuta, T. and Yoshii, A., *Appl. Phys. Lett.* **59**, 3607 (1991).
28. Harmon, E.S., Melloch, M.R., Lundstrom, M.S., and Lovejoy, M.L., *Appl. Phys. Lett.* **83**, 537 (1993).
29. Casey, H.C., SpringThorpe, A.J., "Nonconventional electron diffusion current in GaAs/AlGaAs N-p-n

- heterojunction bipolar transistors with heavily doped base layers", *J. Appl. Phys.* **85**, 6 (1989).
30. Renaud, Ph., Raymond, F., Bensaid, B., and Verie, C., *J. Appl. Phys.* **71** (4), (1992).
 31. Badescu, V. and Landsberg, P.T., *Semicond. Sci. Technol.* **8**, 1267, (1993).
 32. Patkar, Lundstrom, and Melloch, *J. Appl. Phys.*, **78**, (4), (1995).
 33. Casey, Jr., Sell, Wecht, *J. Appl. Phys.*, **46**, (1) (1975).
 34. Asbeck, P., *J. Appl. Phys.*, **48**, (2), (1977).
 35. Pedrotti, Leno, Pedrotti, Introduction To Optics, (New Jersey, Prentice Hall, 1993), pg.514.

INITIAL DISTRIBUTION LIST

1. Defense Technical Information Center
Ft. Belvoir, Virginia
2. Dudley Knox Library
Naval Postgraduate School
Monterey, California
3. Professor Nancy M. Haegel
Naval Postgraduate School
Monterey, CA
4. Professor James Luscombe
Naval Postgraduate School
Monterey, CA
5. Thomas Boone
Hitachi Global Storage
San Jose, CA
6. Dave Luber
Headquarters United States Marine Corps
Washington, DC
7. Rear Admiral Joe Kernan
United States Special Operations Command
Tampa, FL